

## Discussion - Reply

**Cite this article:** Abdel Wanees NG, El-Sayed MM, Khalil KI, and Khamis HA (2022) Petrogenesis of contrasting magmatic suites in the Abu Kharif area, Northern Eastern Desert, Egypt: implications for Pan-African crustal evolution and tungsten mineralization. *Geological Magazine* **159**: 441–467. <https://doi.org/10.1017/S0016756821001047>



Received: 29 October 2020  
Revised: 11 June 2021  
Accepted: 14 September 2021  
First published online: 30 November 2021

**Keywords:**

Pan-African crust; granites; geochemistry; W-mineralization; petrogenetic models; Eastern Egypt Desert

**Author for correspondence:** Nora Gamal Abdel Wanees,  
Email: [n.gamal2017@yahoo.com](mailto:n.gamal2017@yahoo.com)

# Petrogenesis of contrasting magmatic suites in the Abu Kharif area, Northern Eastern Desert, Egypt: implications for Pan-African crustal evolution and tungsten mineralization

Nora G Abdel Wanees<sup>1</sup> , Mohamed M El-Sayed<sup>1</sup> , Khalil I Khalil<sup>2</sup> and Hossam A Khamis<sup>3</sup>

<sup>1</sup>Geology Department, Faculty of Science, Damanhour University, Damanhour, Egypt; <sup>2</sup>Geology Department, Faculty of Science, Alexandria University, Alexandria, Egypt and <sup>3</sup>Nuclear Materials Authority, Maadi, Cairo, Egypt

**Abstract**

The Abu Kharif area in the Northern Eastern Desert consists of contrasting granitic magma suites: a Cryogenian granodiorite suite (850–635 Ma), an Ediacaran monzogranite suite (635–541 Ma) and a Cambrian alkali riebeckite granite suite (541–485 Ma). Tungsten mineralization occurs within W-bearing quartz veins and a disseminated type confined to the monzogranite.

Whole-rock geochemical data classify the granodiorite as a late-orogenic I-type with calc-alkaline affinity, while the monzogranite and alkali riebeckite granite represent respectively a post-orogenic highly fractionated I-type with calc-alkaline affinity and an anorogenic A1-subtype with alkaline affinity. Geochemical modelling indicates that the three intrusions represent separate magmatic pulses where the granodiorite was generated by ~75 % batch partial melting of an amphibolitic source followed by fractional crystallization of hornblende, biotite, apatite and titanite. The monzogranite was formed by 62 % batch partial melting of the normal ‘non-metasomatized’ Pan-African crust of calc-alkaline granite composition followed by fractional crystallization of plagioclase, biotite, K-feldspar, magnetite, ilmenite, with minor apatite and titanite. The alkali riebeckite granite was generated by 65 % batch partial melting of metasomatized Pan-African granite source followed by fractional crystallization of plagioclase, K-feldspar, amphibole and biotite with minor magnetite, apatite and titanite. In general, the parent magmas of the three intrusions were originally enriched in W, but with different concentrations. This W-enrichment would be caused by magmatic-related hydrothermal volatile-rich fluids and concentrated within the monzogranite.

**1. Introduction**

The East African Orogen (EAO), formed by the closure of the Mozambique Ocean, characterizes the most extensive Gondwana-forming orogen (Fig. 1a; Kusky *et al.* 2003; Jacobs & Thomas, 2004; Abu Sharib *et al.* 2019). The northern part of the EAO is represented by the Arabian–Nubian Shield (ANS; Fig. 1a). The EAO basement consists of high-grade metamorphic units in the Mozambique belt, to the south, and of low-grade metamorphic units of volcanic, plutonic and sedimentary origins in the ANS, to the north (Cox *et al.* 2012). The ANS represents a large tract of juvenile crust in northeast Africa and Arabia, which was formed during the Neoproterozoic East African orogenic cycle (*c.* 850–550 Ma; Johnson *et al.* 2013; Yeshanew, 2017). The tectonic evolution of the ANS follows the break-up of Rodinia (~850 Ma; Stern, 1994) during the Cryogenian (850–635 Ma) and Ediacaran (635–541 Ma) periods. The older Cryogenian crust consists of four main units: (i) metavolcano-sedimentary rocks, (ii) dismembered ophiolitic nappes and ophiolitic mélange, (iii) metagabbro–diorite complexes and (iv) quartz diorite–trondhjemite–tonalite–granodiorite intrusions. During the Ediacaran, these units were intruded by felsic A-type granite intrusions. The Pan-African orogenic shield rocks of eastern Egypt were intruded by several anorogenic within-plate granitic complexes, including Mount Abu-Kharif of Cambrian age (522 Ma; Abdel-Rahman, 2006).

Stern and Hedge (1985) subdivided the Eastern Desert into three terranes: the Northern (NED), Central (CED) and Southern Eastern Desert (SED) based on distribution of rock types and their absolute ages (Fig. 1b). The NED is characterized by an abundance of post-orogenic felsic granite intrusions, Dokhan volcanics and molasse-type sediments of the Hammamat Group. Metavolcanics, volcanogenic metasediments and diorite–granodiorite–trondhjemite intrusives are also recorded in a few areas of the NED (Eliwa *et al.* 2014). In the CED, ophiolitic mélanges and arc assemblages predominate, while the SED is characterized by a high proportion

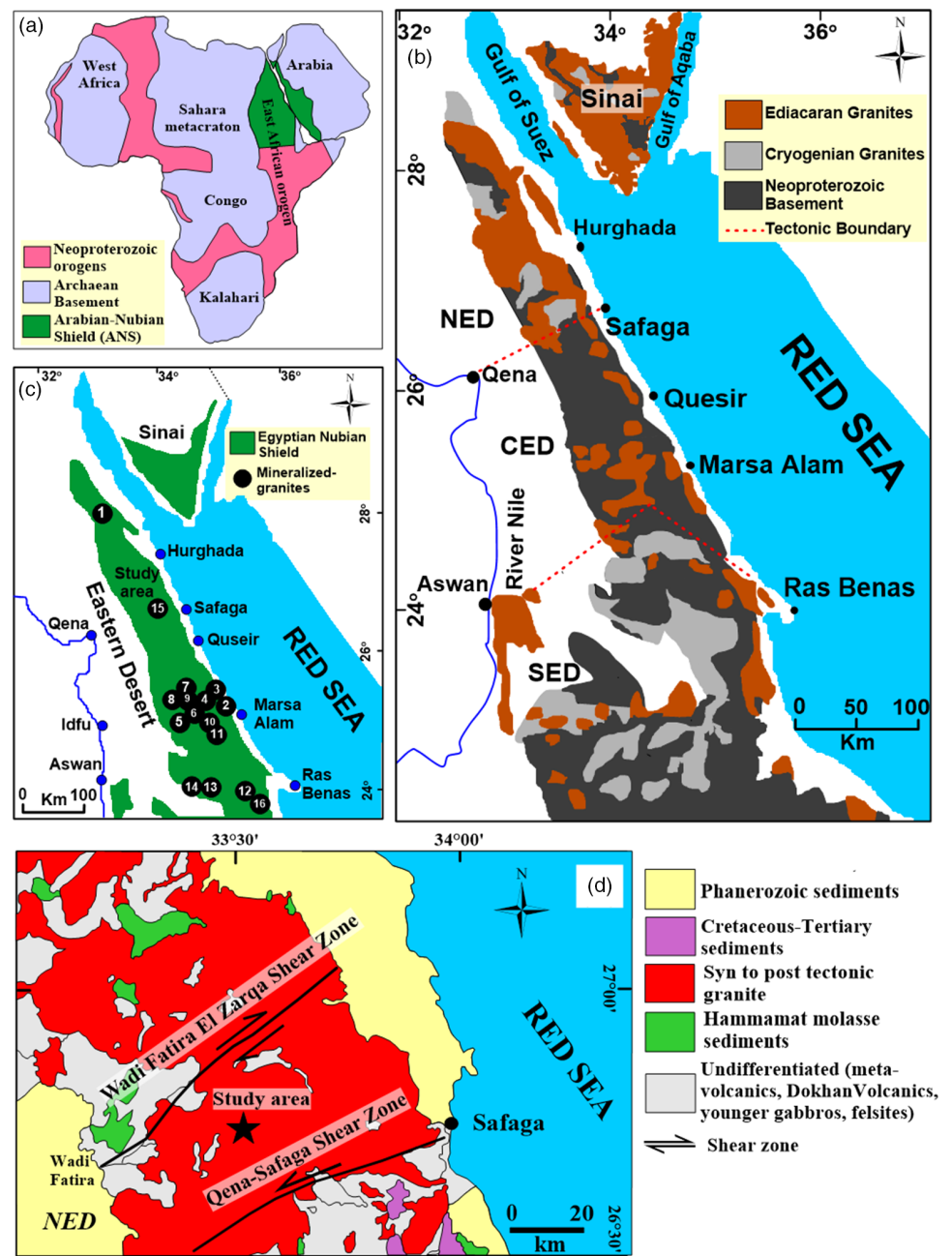


**Fig. 1.** (Colour online) (a) Geographical distribution of the East African Orogen (EAO) in Africa and Arabia. The northern part of the EAO is represented by the Arabian–Nubian Shield (ANS) (modified after Abu Sharib *et al.* 2019). (b) Distribution map of the Egyptian Cryogenian (850–635 Ma) and Ediacaran (635–541 Ma) granites within the Neoproterozoic basement of the Eastern Desert and Sinai (after El-Bialy, 2020). NED, CED and SED represent Northern Eastern Desert, Central Eastern Desert and Southern Eastern Desert, respectively. (c) Location map of the most important mineralized-granitic intrusions in the Eastern Desert of Egypt: 1. Hawashia (Nb, Zr, Y); 2. Igla (Sn, W, Be, Li); 3. Abu Dabbab (Nb, Ta, Sn); 4. Nuweibi (Nb, Ta, Sn); 5. El Mueilha (F, Sn, W); 6. Humr Waggat (Nb, Ta, F); 7. Umm Naggat (Sn, Nb, Ta); 8. Umm Samra (U, W, Nb, Ta); 9. Ineigi (Sn, F); 10. Zabara (Be, Mo, W, Sn); 11. Nugrus (Be); 12. El Gharabiya; 13. Nikeiba (U); 14. Humr Akarem (Mo, Nb, Sn, Bi, F); 15. Abu Kharif (W); 16. Um Desi (Mo). (d) Simplified geological map showing location of the Abu Kharif area between the two mega-shear zones Qena-Safaga and W. Fatira El Zarga (modified after Abd El-Wahed and Abu Anbar, 2009).

of Cryogenian granites and a relatively high abundance of gneisses and migmatites (El Bahariya, 2018; Stern, 2018; Stern & Ali, 2020).

Based on field relations, tectonic and geochronological studies, the Egyptian granites have been subdivided into older ( $\approx 27\%$  by volume) and younger ( $\approx 30\%$  by volume) granites, crystallized during a Cryogenian orogenic stage (850–635 Ma) and an Ediacaran orogenic stage (635–541 Ma), respectively (e.g. El-Sayed, 1998; Akaad & Abu El-Ela, 2002; El-Bialy & Hassen, 2012; Stern, 2018; Stern & Ali, 2020). The predominance of granitic rocks in the Egyptian shield increases northward (Fig. 1b). The Cryogenian granite intrusions are formed by either fractional crystallization of mafic crustal-derived melts generated by melting of the amphibolitic lower crust (Moghazi, 1999; Farahat *et al.* 2007; El-Mahallawi & Ahmed, 2012; Basta *et al.* 2017) or by fractional crystallization of mantle-derived mafic magma with assimilation (Eliwa *et al.* 2014; El-Bialy & Omar, 2015). The Ediacaran

granite intrusions have geochemical characteristics of highly fractionated calc-alkaline I-type granites and A-type granites of alkaline affinity (El-Sayed, 1998; El-Sayed *et al.* 1999; Abd El-Ghaffar & Ramadan, 2018). They are formed by either fractional crystallization of crustal magma (Moghazi *et al.* 2004; Farahat *et al.* 2007; Farahat & Azer, 2011; Ali *et al.* 2012; El-Bialy & Omar, 2015; Lindh *et al.* 2019; Mohamed *et al.* 2019) or by melting of oceanic crust and magma mixing of juvenile mantle-derived magma with felsic crustal melts (Farahat *et al.* 2011; Ali *et al.* 2016; Abdel-Rahman, 2021).

Rare metals such as W, Mo, Sn, Ta, Nb, U, Th, REE and other mineralization in the Nubian Shield are commonly associated with the post-collision Ediacaran A-type granites and have a spatial connection with fault zones (Helba *et al.* 1997; Moghazi *et al.* 2015). Sixteen localities of mineralized granites have been discovered and/or mined in the Eastern Desert of Egypt (Fig. 1c). The

geological importance of the Abu Kharif area lies in the occurrence of contrasting granitic magmas of granodiorite, monzogranite and alkali riebeckite granite. In addition, the monzogranite is tungsten-bearing granite.

In this paper we present new whole-rock major, trace and rare earth element data for samples collected from the different granite rock types in the Abu Kharif area. These data precisely constrain the magmatic suites and allow us to investigate the tectonic setting, petrogenesis and magma source of these granites. Additionally, some samples of the studied granite intrusions contain high W contents while other granitic samples are barren. Thus, the effective mechanism for the formation of tungsten mineralization and the factors controlling the distribution of W are also discussed.

## 2. Geological setting and W-mineralization

The Abu Kharif area lies in the Northern Eastern Desert of Egypt at 33° 21'–33° 28' E, 26° 47'–26° 50' N (Fig. 2a). The area is covered by different magmatic units including metavolcanics, granodiorite, monzogranite and alkali riebeckite granite (Fig. 2a, b). All these rocks, except the alkali riebeckite granite, are commonly intruded by dolerite dykes and quartz veins. The intrusive contacts between the different granitic rocks as well as with the metavolcanic wall-rock units are sharp.

The metavolcanic unit is interpreted as related to a Cryogenian subduction event, and consists of the oldest rock unit in the study area. They are heterogeneous, showing prominent variations in colour index, grain-size and proportions of the constituting mineral phases. They are composed of acidic (metadacite and metarhyolite) and basic (metabasalt) metavolcanic successions; the latter are weakly foliated at greenschist facies. Sharp contact is observed between the basic and acidic metavolcanics. Locally, the metavolcanics are associated with some interbeds and lenses of metapetroclastic rocks.

Granodiorite comprises the most abundant variety in the study area (Fig. 2a). It is a homogeneous, coarse-grained and equigranular rock. The investigated granodiorite displays most of the chemical and field characteristics of late-tectonic I-type granites described elsewhere in the Eastern Desert of Egypt (~650 Ma; Moghazi, 1999; El-Shazly & El-Sayed, 2000). The granodiorite is dissected by dyke swarms of basic composition, although felsic varieties do exist. The rock surfaces are commonly exfoliated, which could be attributed to their coarse grain-size. Medium-grained massive and irregular rounded to sub-rounded mafic xenoliths of amphibolitic composition with an average diameter of a few tens of centimetres scale are scattered in sharp contacts against the host granodiorite. The granodiorite intrudes the metavolcanics at Valley Kahaly. It is intruded in sharp contacts by the monzogranite and the alkali riebeckite granite (Fig. 3a).

The monzogranite lies to the south of Mount Abu Kharif (Fig. 2a). It clearly intrudes the metavolcanic and granodiorite rock units with mutual sharp contacts. The Ediacaran monzogranite has similar field, petrographical and chemical characters to the highly fractionated I-type post-orogenic intrusive granites (610–580 Ma; Moghazi, 1999; Mahdy *et al.* 2015; Sami *et al.* 2018) distributed in the Eastern Desert of Egypt. It forms moderate to low smooth topography and is deeply weathered. Exfoliation structure and joints are common. The monzogranite is medium- to coarse-grained, and ranges in colour from whitish-pink to pale pink with joint sets oriented mainly N–S and NE–SW. It is characterized by the presence of oval-shaped, grey-color dioritic xenoliths with different dimensions. The dioritic xenoliths consist mainly of

plagioclase and green actinolite, with secondary chlorite, ilmenite and apatite. The monzogranite is injected by a set of W-bearing quartz veins particularly at the south of Mount Abu Kharif (Fig. 3b, c).

The alkali riebeckite granite has a Cambrian age ( $522 \pm 21$  Ma; Abdel-Rahman, 2006) dated in the Abu Kharif area. It is classified as A-type anorogenic intrusive plutons (El-Sayed, 1998; Abdel-Rahman, 2006). The rough mountainous ridges of the alkali riebeckite granite show intrusive sharp contacts with most of the surrounding country rocks (Fig. 3d). The alkali riebeckite granite is leucocratic, medium- to coarse-grained, with pink to red colour. It is worth noting that this granite type is not dissected by any dykes and/or veins.

The tungsten mineralization in the Abu Kharif area occurs as wolframite-bearing quartz veins and disseminated in the wall rock (Fig. 3b, c). The mineralized quartz veins and veinlets show variable thickness ranging from a few centimetres up to 3 m. They are confined to an area ~350 m wide and 600 m long in the monzogranite pluton with average W content of 64.79 ppm. The surrounding alteration haloes show W content of 15.08 ppm, on average (El-Desouky, 2005). The quartz veins generally form steep walls and sharp contacts against the host monzogranite. The mineralized veins are clustered in two zones: the northern zone is highly mineralized with wolframite unlike the southern zone. The northern ore zone comprises around 15 quartz veins generally striking E–W and NE–SW with dip angles between 30 and 50°, towards either N–S or NW–SE (Fig. 3b). However, the southern zone includes a series of veins and veinlets striking to E–W and NE–SW and dipping at angles 30–40° to the N. The distribution of mineralized veins is controlled by the conspicuous NE–SW large-scaled and wide dextral shear zones (Fig. 1d) in addition to some minor fault predominated in the monzogranite. On the other hand, the NNW–SSE fault trend is cut through the alkali riebeckite granite (Fig. 2a, b).

Generally, the wolframite-bearing quartz veins and veinlets are fine- to medium-grained milky quartz which represents up to 95 % of the vein mode. The quartz occurs as large euhedral crystals (up to  $3 \times 1$  cm) in addition to anhedral crystals filling cavities between the euhedral quartz crystals. Wolframite and sulphides occur as disseminated grains in the quartz veins, sometimes in the form of nests (Fig. 3c). These veins post-date the host granite intrusions and seem to be formed by Na-rich hydrothermal fluids (Abdel-Rahman, 2006). The wolframite-bearing quartz veins are associated with extensive alkali alteration superposed by greisenization and silicification. Disseminated wolframite is present in alteration zones.

## 3. Petrography

### 3.a. Granodiorite

The granodiorite of equigranular texture consists of plagioclase (53 vol. %), quartz (15 vol. %), K-feldspar (13 vol. %), hornblende (9 vol. %), biotite (6 vol. %), with limited amounts of secondary chlorite, epidote and sericite. Accessory minerals are mainly titanite and apatite. Plagioclase has oligoclase composition ( $An_{15-20}$ ), commonly euhedral to subhedral tabular and prismatic crystals with grain-size up to 4.5 mm in length and 2 mm in width. Plagioclase crystals frequently display carlsbad twinning. The large plagioclase crystals are characterized by numerous inclusions of quartz and hornblende. Plagioclase crystals are commonly altered to sericite. Quartz exists as anhedral granular grains showing

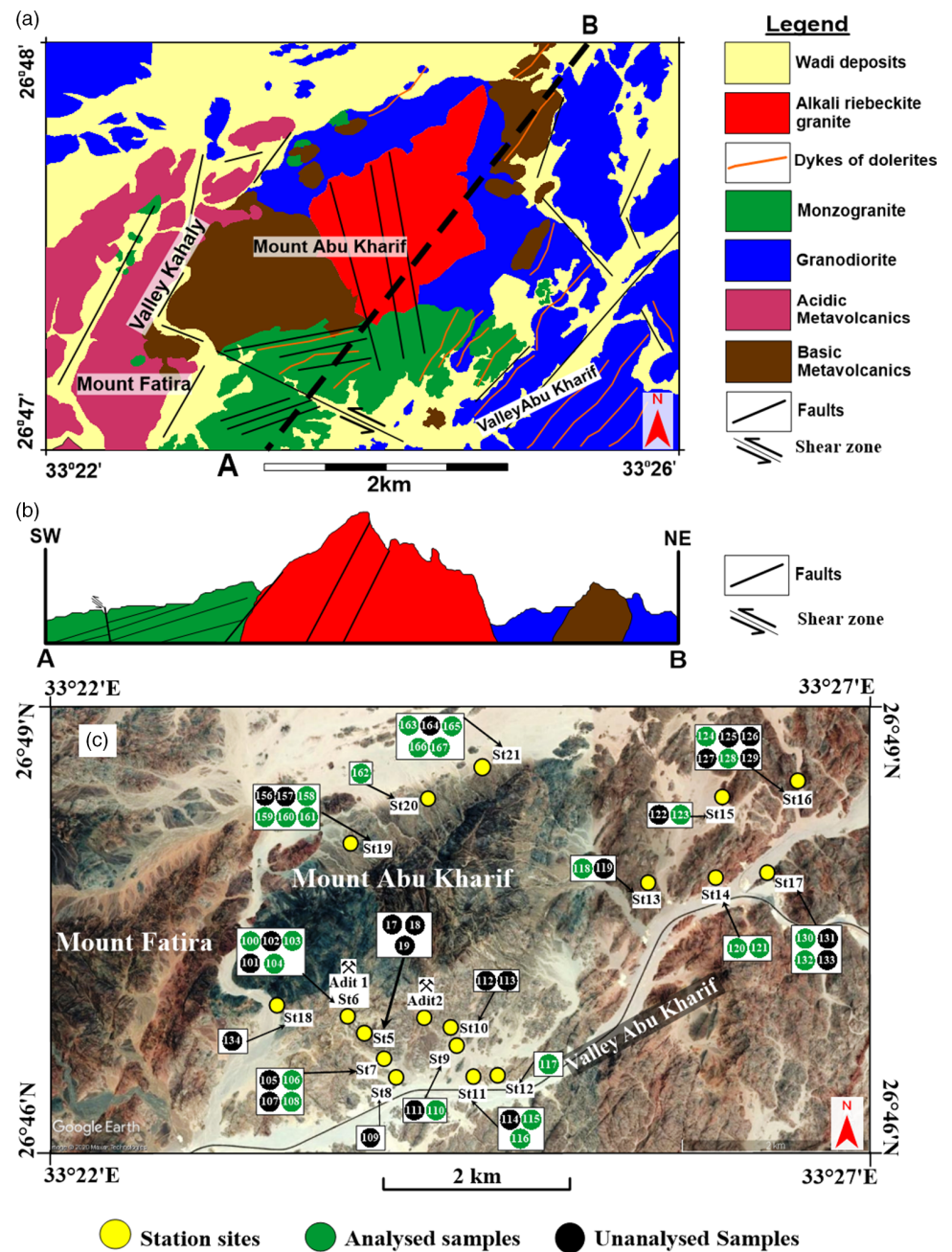


**Fig. 2.** (Colour online) (a) Geological map of the Abu Kharif area. (b) Schematic cross-section diagram along A–B line showing the rock units and structural elements in the study area. (c) Satellite image (Google Earth) showing the different sites and sample locations in the study area.

undulose extinction and cracks. Quartz occasionally occurs as small crystal inclusions in orthoclase, giving graphic and micrographic textures (Fig. 4a). K-feldspars are represented mainly by orthoclase, whereas microcline is rarely observed. K-feldspars are subhedral to anhedral tabular crystals with dimensions up to 1.4 mm in length and 0.6 mm in width. Myrmekitic texture appears at the contact between K-feldspars and plagioclase crystals (Fig. 4b). Biotite occurs as prisms or irregular tabular flakes up to 3 mm in diameter. Biotite is partially or completely altered to chlorite  $\pm$  opaques along cleavage planes. Subhedral to anhedral hornblende crystals range in colour from brown to green and are medium- to fine-grained up to 2 mm in length and 1.4 mm in width. Sometimes hornblende is altered to chlorite and appears associated with epidote, titanite and iron oxides. Titanite is a relatively abundant accessory mineral and occurs as an alteration

product of the iron oxides as well as rhombic-shaped primary magmatic titanite. Apatite occurs as short euhedral prismatic crystals enclosed in plagioclase, biotite and hornblende. Iron oxides are present as small irregular grains randomly scattered throughout the rock.

### 3.b. Monzogranite

Monzogranite is leucocratic with porphyritic texture and is characterized by the presence of oval-shaped xenoliths of monzodioritic composition. Monzogranite consists of K-feldspar (39 vol. %), quartz (20 vol. %), plagioclase (28 vol. %) and a small amount of biotite (10 vol. %). Chlorite, sericite and epidote are secondary minerals, whereas accessories are titanite, zircon, apatite and iron oxide.

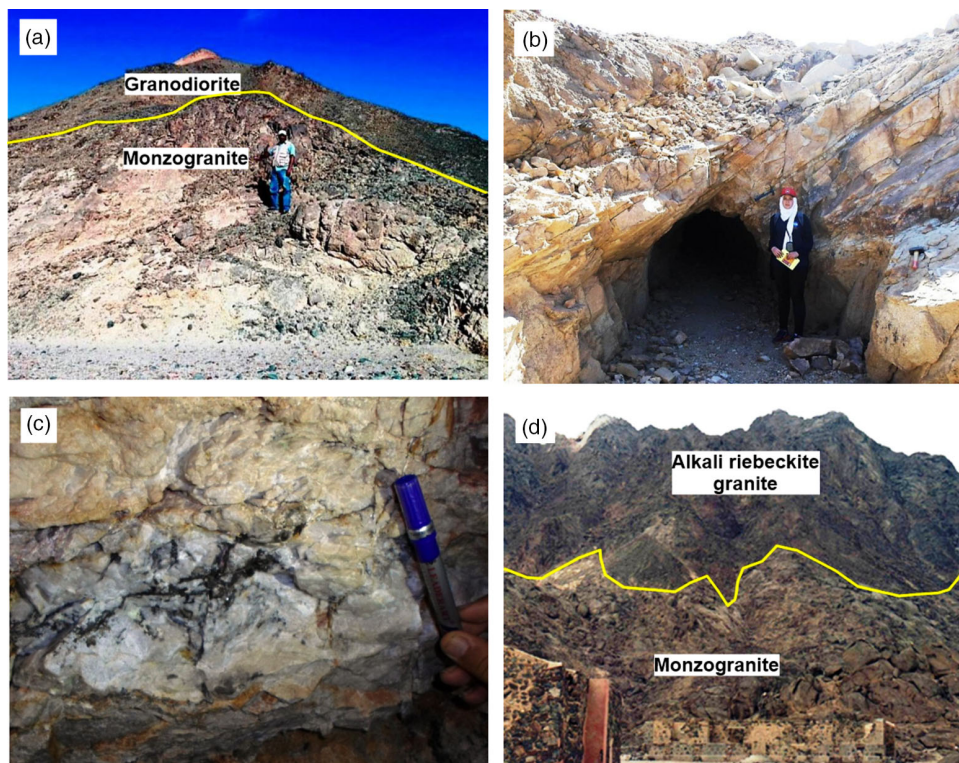


**Fig. 3.** (Colour online) (a) Intrusive contact between the monzogranite and the granodiorite in the Abu Kharif area, looking N. (b) Mineralized quartz vein confined to NE intensively altered shear zone, northern ore zone, looking NE. (c) Wolframite mineralization nested in milky quartz vein that displays vuggy structure. (d) The alkali riebeckite granites intrude the monzogranites with sharp contact, looking SW.

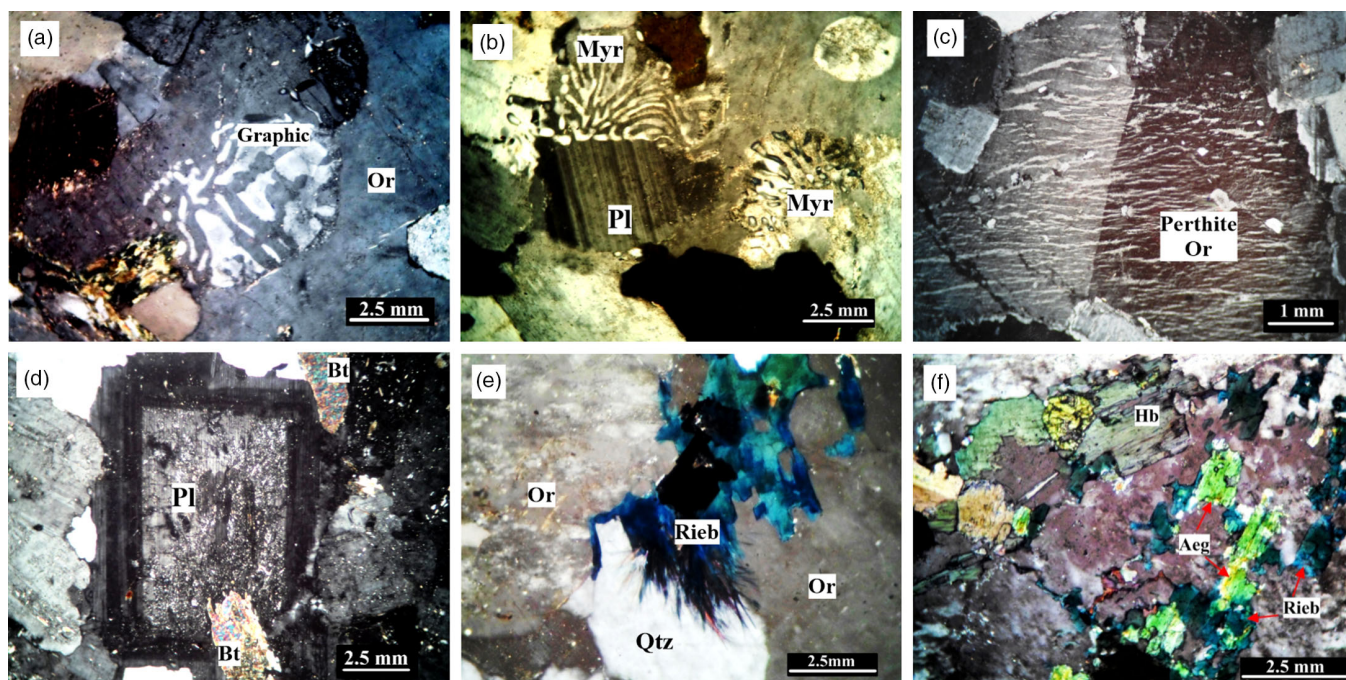


**Fig. 4.** (Colour online) Photomicrographs of (a) graphic intergrowth texture of quartz in orthoclase (Or) (granodiorite), crossed-nicols (XPL); (b) myrmekitic texture (Myr) (granodiorite), Pl = plagioclase, XPL; (c) perthitic texture in orthoclase (Or) with carlsbad twinning (monzogranite), XPL; (d) zoned plagioclase crystal (Pl) altered to kaolinite and sericite in the core (monzogranite), Bt = biotite, XPL; (e) acicular riebeckite (Rieb) showing indigo blue interference colour (alkali riebeckite granite), Or = orthoclase, Qtz = quartz, XPL; (f) emerald green aegirine (Aeg) associated with riebeckite (Rieb) and hornblende (Hb) (alkali riebeckite granite), XPL.

K-feldspar of perthitic texture (vein-, flame-like; Fig. 4c) is the most abundant mineral. The K-feldspar crystals are tabular and most of them are turbid and clouded with clay minerals and/or sericite. Plagioclase (An<sub>11-23</sub>) occurs as medium-grained subhedral crystals with an average of 2 mm in diameter. Most plagioclase

crystals show well-developed albite and carlsbad twinning. Some zoned plagioclase crystals display a sieve texture where the cores are more altered than the rims to sericite (Fig. 4d). Quartz is subhedral to anhedral coarse-grained up to 5.5 mm in diameter. Quartz also occurs as fine-grained anhedral grains in the form

of aggregates. Biotite commonly occurs as subhedral to anhedral flakes with zircon, apatite and muscovite inclusions, while some of the biotite grains are partially altered to chlorite.

### 3.c. Alkali riebeckite granite

The alkali riebeckite granite has an equigranular texture; it consists of K-feldspar (56 vol. %) and quartz (30 vol. %) with rare plagioclase (5 vol. %). Amphiboles are represented by riebeckite and hornblende (5 vol. %), while pyroxene exists in the form of aegirine (1 vol. %). Accessory minerals are zircon and iron oxides. K-feldspar occurs as coarse- and medium-grained subhedral crystals up to 6 mm in length and 3.5 mm in width. K-feldspar crystals display flame-, vein- and patch-like perthitic cross-hatched microcline. Sometimes, K-feldspar is intergrown in plagioclase, forming antiperthite. Quartz often occurs as coarse-grained anhedral crystals of oval and globular shapes and fills the interstitial spaces between K-feldspar grains. Riebeckite and hornblende are coarse-grained, subhedral to anhedral prismatic and strongly pleochroic. Some riebeckite crystals occur as acicular aggregates (Fig. 4e). Emerald green pleochroic grains of aegirine are present, associated with hornblende and riebeckite (Fig. 4f). Subhedral crystals of plagioclase show albitic composition ( $An_{10-15}$ ), and occur in prismatic form. Some twinned and zoned plagioclase crystals display sieve texture showing altered cores in contrast to the relatively fresh rims.

## 4. Geochemistry

### 4.a. Analytical techniques

Whole-rock chemical analyses of 26 representative samples (Fig. 2c), mostly from the least altered and fresh granites, were carried out in the Abu Kharif study area (eight samples of granodiorite, eight samples of monzogranite, nine samples of alkali riebeckite granite and one from a xenolith within monzogranite). Major oxides were analysed at the central laboratories of the Egyptian Mineral Resources Authority, Cairo, Egypt, using Philips X-ray fluorescence spectrometer (XRF) model PW2404 equipped with an Rh radiation tube operated at 40 kV and 70 mA and six analysing crystals (LIF-200, LIF-220, TIAP, Ge, PET, PXL). The analysed element concentrations were determined using Super Q and Semi Q software programs with 99.99 % accuracy and 96.7 % confidence limit. Loss-on-ignition (LOI) was calculated by heating 3 g of rock powder in a porcelain crucible at about 1000 °C for 4 hours. The difference between initial and final weights was used to compute the weight per cent total volatile content of the rock.

On the other hand, the trace and rare earth elements were analysed at the Acme analytical laboratories, Canada, using inductively coupled plasma mass spectrometry (ICP-MS). The accuracy and precision of the analytical results are in the range 1–3 % for major elements and less than 3 % for trace elements. The results of the chemical analyses are given in Tables 1, 2.

### 4.b. Results

#### 4.b.1. Major and trace elements

On the R1–R2 classification diagram (De la Roche *et al.* 1980), granites from the three intrusions plot in granodiorite, granite and alkali granite fields. Exceptions are two samples (# 124 and 108) which plot in tonalite fields (Fig. 5a). On the QAP ternary diagram of Streckeisen (1974), the studied samples were plotted in the granodiorite, monzogranite and alkali-feldspar granite fields

(Fig. 5b). The studied Abu Kharif granite rock types have low normative corundum contents (<1 %). The A-B multi-cationic diagram of Debon and Le Fort (1983) shows the distinct metaluminous character of all the granodiorite samples except for one sample which shows peraluminous affinity (Fig. 5c). On the other hand, the monzogranite samples vary from peraluminous to slightly metaluminous while the alkali riebeckite granite samples are metaluminous except for one sample (# 153) located in the peraluminous domain. According to the plotting position of monzogranite and alkali riebeckite granite, they form an aluminous association (leucogranite field), while the granodiorite forms a caferic association (field IV) (Fig. 5c).

The studied granite types show some significant differences in major- and trace-element composition, particularly in the case of the granodiorite relative to the monzogranite and the alkali riebeckite granite (Tables 1, 2; Fig. 6). For all the granite rock types, the variation diagrams do not show continuous coherent trends for major- and trace-element concentrations (Fig. 6). Additionally, there is a compositional gap (69–74 wt %  $SiO_2$ ) between the granodiorite and both the monzogranite and the alkali riebeckite granite (Fig. 6).

Major-elements Harker diagrams (Fig. 6) for the granodiorite, monzogranite and alkali riebeckite granite show that the  $Al_2O_3$ ,  $FeO^*$ ,  $TiO_2$  and CaO oxides have well-defined negative correlation with  $SiO_2$ . The  $Na_2O$  versus  $SiO_2$  plot shows scattered trends for the granodiorite and a negative trend for the monzogranite and the alkali riebeckite granite. On the  $K_2O$  versus  $SiO_2$  plot, the granodiorite and the monzogranite samples have a slightly positive correlation while the alkali riebeckite granite samples show a slightly negative trend (Fig. 6). The MgO versus  $SiO_2$  diagram shows that the granodiorite and the monzogranite samples correlated negatively with silica while there is no variation in the alkali riebeckite granite samples (Fig. 6). On the  $P_2O_5$  versus  $SiO_2$  plot, the granodiorite samples have negative correlation, while the monzogranite and the alkali riebeckite granite are nearly unchanged with silica variation due to very low contents (Fig. 6).

For the trace elements, the variation diagrams of the granodiorite show that the elements Ba and Sr have negative correlation with silica while Zr has positive correlation (Fig. 6). On the other hand, Nb, Rb and Y values are nearly constant as silica increases (Fig. 6). For the monzogranite, Rb, Nb, Y and Zr are correlated negatively with  $SiO_2$  while Ba has a slightly positive correlation. The Sr– $SiO_2$  plot shows a scattered trend (Fig. 6). Ba and Rb Harker diagrams for the alkali riebeckite granites display decreasing trends with increasing silica while Nb and Y diagrams have positive trends. On the other hand, Sr and Zr diagrams show scattered behaviour (Fig. 6). Additionally, many samples of the studied granite plutons contain high W contents. The average contents of W in the granodiorite, monzogranite and alkali riebeckite granite are 8.11 ppm, 4.3 ppm and 2.53 ppm, respectively (Table 2). One xenolith sample in monzogranite displays 6.7 ppm W content (Table 2).

Following the classifications of Dewitt (1989) and Frost *et al.* (2001) (Fig. 7a, b, respectively), the granodiorite is very Mg-rich while the monzogranite has a wide range between Mg-rich and Fe-rich except for one sample which plots in the field of very Fe-rich. On the other hand, the alkali riebeckite granite is characterized by high  $Fe^\#$  (0.99–1.00) and plots in the very Fe-rich field (Fig. 7a, b).

In the  $(Na_2O + K_2O - CaO)$  vs  $SiO_2$  diagram of Frost and Frost (2008), the granodiorite plots in the calcic field, whereas the monzogranite is restricted to the calc-alkalic field. On the other hand, the alkali riebeckite granite samples straddle the alkali-calcic and

**Table 1.** Major oxides (wt %) and trace-element (ppm) values of the Abu Kharif granitoid rock types

Sample	132	130	128	124	123	121	120	118	Avg.	117	116	115	110	106	104	103	100	Avg.
Litho.	Granodiorite									Monzogranite								
<b>SiO<sub>2</sub></b>	69.63	67.93	66.96	64.87	67.59	65.99	66.80	68.80	<b>67.32</b>	77.22	76.88	77.59	74.96	75.07	76.18	75.11	75.70	<b>76.09</b>
<b>TiO<sub>2</sub></b>	0.47	0.50	0.56	0.62	0.60	0.60	0.55	0.55	<b>0.56</b>	0.14	0.11	0.13	0.24	0.22	0.18	0.23	0.21	<b>0.18</b>
<b>Al<sub>2</sub>O<sub>3</sub></b>	13.98	14.69	15.06	15.41	14.47	14.13	14.81	14.01	<b>14.57</b>	12.19	12.27	12.25	12.84	12.97	12.85	13.06	12.81	<b>12.66</b>
<b>Fe<sub>2</sub>O<sub>3</sub>*</b>	3.64	3.75	3.97	4.41	3.90	4.64	4.25	3.81	<b>0.73</b>	0.99	1.07	0.80	1.53	1.46	1.17	1.38	1.25	<b>0.22</b>
<b>FeO</b>	2.69	2.77	2.93	3.25	2.88	3.42	3.14	2.81	<b>2.99</b>	0.73	0.79	0.59	1.13	1.08	0.86	1.02	0.92	<b>0.89</b>
<b>MnO</b>	0.01	0.01	0.01	0.01	0.01	0.01	0.01	0.01	<b>0.01</b>	0.01	0.01	0.01	0.01	0.01	0.01	0.01	0.01	<b>0.01</b>
<b>MgO</b>	1.59	2.01	2.23	2.58	2.30	2.56	2.34	1.78	<b>2.17</b>	0.03	0.01	0.06	0.38	0.41	0.09	0.28	0.29	<b>0.19</b>
<b>CaO</b>	3.58	3.87	4.12	4.71	4.08	4.06	4.30	4.00	<b>4.09</b>	0.87	0.69	0.68	1.23	1.17	0.91	1.01	0.85	<b>0.93</b>
<b>Na<sub>2</sub>O</b>	4.20	4.30	4.32	4.06	4.04	3.91	4.17	3.96	<b>4.12</b>	3.87	4.29	3.99	3.95	4.12	4.08	4.19	4.15	<b>4.08</b>
<b>K<sub>2</sub>O</b>	1.94	1.81	1.51	1.61	0.14	1.61	1.67	1.55	<b>1.48</b>	3.91	3.82	3.99	3.95	3.91	3.87	3.82	3.72	<b>3.87</b>
<b>P<sub>2</sub>O<sub>5</sub></b>	0.10	0.13	0.14	0.22	0.14	0.16	0.15	0.11	<b>0.14</b>	0.01	0.01	0.01	0.06	0.03	0.01	0.02	0.01	<b>0.02</b>
<b>LOI</b>	0.55	0.70	0.82	1.19	0.92	2.02	0.65	1.11	<b>1.00</b>	0.47	0.61	0.60	0.54	0.33	0.35	0.58	0.69	<b>0.52</b>
<b>Total</b>	<b>99.41</b>	<b>99.41</b>	<b>99.39</b>	<b>99.36</b>	<b>97.89</b>	<b>99.34</b>	<b>99.37</b>	<b>99.41</b>	<b>99.20</b>	<b>99.67</b>	<b>99.70</b>	<b>100.06</b>	<b>99.59</b>	<b>99.61</b>	<b>99.62</b>	<b>99.60</b>	<b>99.61</b>	<b>99.68</b>
<b>DC1</b>	6.48	7.78	8.70	9.58	11.68	9.48	8.70	7.91	<b>8.79</b>	1.83	1.14	1.83	2.14	2.12	1.54	1.82	2.23	<b>1.83</b>
<b>DC2</b>	2.32	2.86	3.48	3.78	5.87	2.82	3.08	3.34	<b>3.44</b>	-0.09	-0.56	-0.09	0.01	-0.08	0.17	0.07	0.20	<b>-0.05</b>
<b>Ba</b>	411.00	427.00	456.00	465.00	413.00	473.00	437.00	320.00	<b>425.25</b>	201.00	759.00	570.00	660.00	537.00	529.00	509.00	461.00	<b>528.25</b>
<b>Be</b>	1.00	2.00	1.00	2.00	1.00	1.00	2.00	1.00	<b>1.38</b>	7.00	1.00	1.00	4.00	1.00	2.00	3.00	3.00	<b>2.75</b>
<b>Co</b>	10.60	12.10	12.50	12.70	11.50	14.70	12.50	11.30	<b>12.24</b>	9.90	1.50	1.60	10.00	2.70	2.20	2.00	2.00	<b>2.86</b>
<b>Cs</b>	0.70	0.60	0.70	0.20	0.70	0.50	0.40	0.50	<b>0.54</b>	9.10	1.50	0.90	1.70	2.30	2.20	3.10	2.30	<b>2.89</b>
<b>Ga</b>	17.60	18.10	17.50	17.60	17.60	16.90	17.70	16.70	<b>17.46</b>	24.20	15.70	17.00	16.30	17.30	16.80	17.50	18.10	<b>17.86</b>
<b>Hf</b>	4.10	3.60	4.00	2.80	4.80	3.40	3.90	5.20	<b>3.98</b>	4.60	2.70	3.50	2.90	3.90	5.10	4.00	4.30	<b>3.88</b>
<b>Nb</b>	3.30	3.50	3.40	3.40	3.80	3.80	3.40	2.60	<b>3.40</b>	39.70	7.40	13.40	10.10	14.50	15.20	15.90	17.80	<b>16.75</b>
<b>Rb</b>	32.70	32.20	24.20	29.30	33.10	26.60	29.20	24.30	<b>28.95</b>	124.90	96.20	101.40	97.20	102.80	102.90	134.20	105.60	<b>108.15</b>
<b>Sn</b>	1.00	1.00	1.00	1.00	1.00	1.00	1.00	1.00	<b>1.00</b>	5.00	1.00	1.00	1.00	2.00	2.00	2.00	2.00	<b>2.00</b>
<b>Sr</b>	650.80	640.00	695.80	714.20	641.60	760.00	713.10	678.80	<b>686.79</b>	429.30	255.10	212.50	232.60	238.20	236.60	195.30	208.10	<b>250.96</b>
<b>Ta</b>	0.20	0.30	0.20	0.30	0.30	0.20	0.20	0.30	<b>0.25</b>	3.00	0.60	1.50	0.80	1.10	1.10	1.40	1.60	<b>1.39</b>
<b>Th</b>	4.10	4.70	3.50	2.50	4.80	4.30	5.00	5.20	<b>4.26</b>	19.00	6.90	9.00	7.50	9.30	12.80	11.80	8.60	<b>10.61</b>
<b>U</b>	1.20	1.50	1.00	0.70	1.70	1.40	1.30	1.20	<b>1.25</b>	6.10	2.70	3.90	3.40	2.40	2.90	3.70	2.30	<b>3.43</b>
<b>V</b>	680	70.00	83.00	80.00	75.00	94.00	83.00	79.00	<b>79.00</b>	80.00	13.00	14.00	14.00	27.00	29.00	25.00	34.00	<b>29.50</b>
<b>W</b>	1.60	1.60	1.60	1.60	1.60	46.40	4.60	5.90	<b>8.11</b>	4.80	5.60	4.00	4.00	4.00	4.00	4.00	4.00	<b>4.30</b>
<b>Zr</b>	146.50	139.20	163.90	103.80	195.90	137.70	148.40	214.90	<b>156.29</b>	139.40	80.10	83.20	78.10	129.20	168.10	115.50	137.20	<b>116.35</b>
<b>Y</b>	11.90	12.80	13.00	11.30	13.40	14.30	13.50	11.20	<b>12.68</b>	19.50	6.60	12.40	8.20	12.40	13.60	12.30	15.60	<b>12.58</b>

Sample	167	166	165	163	162	161	160	159	158	Avg.	108
Lithology	Alkali riebeckite granite										Xenolith
<b>SiO<sub>2</sub></b>	76.65	77.81	75.93	76.87	79.65	75.73	75.45	77.38	79.83	<b>77.26</b>	64.50
<b>TiO<sub>2</sub></b>	0.17	0.15	0.19	0.17	0.16	0.24	0.25	0.17	0.10	<b>0.18</b>	0.77
<b>Al<sub>2</sub>O<sub>3</sub></b>	11.30	11.17	11.77	11.58	9.89	11.95	12.04	11.20	10.33	<b>11.25</b>	15.36
<b>Fe<sub>2</sub>O<sub>3</sub>*</b>	2.40	2.01	2.50	2.25	2.22	2.58	2.52	2.39	1.99	<b>0.42</b>	1.25
<b>FeO</b>	1.77	1.48	1.84	1.66	1.64	1.90	1.86	1.76	1.47	<b>1.71</b>	3.55
<b>MnO</b>	0.01	0.01	0.01	0.01	0.01	0.01	0.01	0.01	0.01	<b>0.01</b>	0.03
<b>MgO</b>	0.01	0.01	0.01	0.01	0.01	0.01	0.01	0.01	0.01	<b>0.01</b>	2.41
<b>CaO</b>	0.26	0.11	0.19	0.11	0.15	0.49	0.59	0.16	0.01	<b>0.23</b>	3.12
<b>Na<sub>2</sub>O</b>	4.12	4.04	4.31	4.22	3.60	4.28	4.25	4.06	3.54	<b>4.05</b>	5.35
<b>K<sub>2</sub>O</b>	4.55	4.49	4.60	4.65	3.87	4.22	4.10	4.33	3.91	<b>4.30</b>	2.02
<b>P<sub>2</sub>O<sub>5</sub></b>	0.01	0.01	0.01	0.01	0.01	0.01	0.02	0.01	0.01	<b>0.01</b>	0.24
<b>LOI</b>	0.60	0.29	0.54	0.22	0.49	0.34	0.55	0.31	0.43	<b>0.42</b>	0.69
<b>Total</b>	<b>99.90</b>	<b>99.95</b>	<b>99.87</b>	<b>99.94</b>	<b>99.90</b>	<b>99.67</b>	<b>99.60</b>	<b>99.86</b>	<b>100.03</b>	<b>99.86</b>	<b>98.91</b>
<b>DC<sub>1</sub></b>	-1.85	-0.66	-1.86	-1.50	0.79	-1.29	-0.97	-0.89	1.10	<b>-0.79</b>	5.82
<b>DC<sub>2</sub></b>	-3.24	-2.81	-3.36	-3.25	-2.15	-2.58	-2.20	-2.83	-1.57	<b>-2.67</b>	0.29
<b>Ba</b>	83.00	72.00	100.00	98.00	79.00	317.00	354.00	85.00	40.00	<b>136.44</b>	459.00
<b>Be</b>	4.00	4.00	4.00	3.00	6.00	3.00	2.00	3.00	2.00	<b>3.44</b>	2.00
<b>Co</b>	0.20	0.20	0.20	0.20	0.20	2.00	1.10	0.60	0.40	<b>0.57</b>	1.90
<b>Cs</b>	0.10	0.10	0.30	0.10	0.20	0.60	1.30	0.20	0.20	<b>0.34</b>	2.00
<b>Ga</b>	27.60	26.80	28.30	28.70	24.00	25.30	24.80	27.60	24.30	<b>26.38</b>	17.40
<b>Hf</b>	13.40	14.60	13.60	13.40	16.00	12.70	12.40	17.10	15.10	<b>14.26</b>	4.50
<b>Nb</b>	56.10	55.60	62.20	63.10	63.10	50.20	47.30	62.20	78.50	<b>59.81</b>	15.60
<b>Rb</b>	60.60	54.30	55.50	56.30	50.20	72.00	67.50	61.50	85.00	<b>62.54</b>	109.60
<b>Sn</b>	3.00	3.00	3.00	3.00	3.00	5.00	5.00	4.00	6.00	<b>3.89</b>	2.00
<b>Sr</b>	8.40	7.60	9.60	9.40	9.80	62.50	59.00	13.10	18.00	<b>21.93</b>	192.10
<b>Ta</b>	2.80	3.10	3.10	3.10	3.70	3.50	3.20	4.60	4.70	<b>3.53</b>	1.20
<b>Th</b>	6.90	7.70	7.70	7.80	9.60	10.70	9.90	9.10	12.00	<b>9.04</b>	10.90
<b>U</b>	1.90	2.10	1.90	1.90	2.20	2.30	1.70	2.30	3.40	<b>2.19</b>	2.60
<b>V</b>	8.00	8.00	8.00	8.00	8.00	12.00	9.00	8.00	8.00	<b>8.56</b>	34.00
<b>W</b>	2.00	2.00	2.00	2.00	2.00	2.00	4.00	2.00	4.80	<b>2.53</b>	6.70
<b>Zr</b>	681.40	673.30	646.80	603.00	679.50	509.60	492.60	685.50	472.40	<b>604.90</b>	138.10
<b>Y</b>	52.70	56.40	58.50	56.90	62.70	53.90	51.20	57.80	80.60	<b>58.97</b>	13.60

Fe<sub>2</sub>O<sub>3</sub>\* = total iron as ferric; DC<sub>1</sub> and DC<sub>2</sub> = discrimination parameters of Agrawal (1995).



**Table 2.** Rare earth elements (ppm) values of the Abu Kharif granitoid rock types

Sample	132	130	128	124	123	121	120	118	Avg.	117	116	115	110	106	104	103	100	Avg.
Lithology	Granodiorite									Monzogranite								
<b>La</b>	19.50	20.80	27.10	23.40	19.70	22.70	23.10	20.70	<b>22.13</b>	26.90	30.30	25.20	26.40	26.60	18.80	20.30	19.20	<b>24.21</b>
<b>Ce</b>	44.60	46.80	55.40	52.40	43.70	48.60	48.00	45.00	<b>48.06</b>	50.50	58.40	42.90	48.10	48.60	34.30	37.60	35.80	<b>44.53</b>
<b>Pr</b>	5.94	6.13	6.95	6.73	5.49	6.08	5.87	5.55	<b>6.09</b>	5.35	6.15	4.60	5.29	5.14	3.73	4.07	3.90	<b>4.78</b>
<b>Nd</b>	25.00	25.80	27.70	26.40	21.50	24.50	23.50	22.00	<b>24.55</b>	17.80	19.50	15.20	18.00	17.00	12.90	13.80	13.70	<b>15.99</b>
<b>Sm</b>	4.47	4.80	4.94	4.75	4.12	4.34	4.22	4.01	<b>4.46</b>	3.00	3.55	2.57	3.12	2.93	2.18	2.61	2.20	<b>2.77</b>
<b>Eu</b>	1.49	1.32	1.39	1.41	1.31	1.27	1.10	1.12	<b>1.3</b>	0.63	0.70	0.51	0.61	0.61	0.50	0.43	0.48	<b>0.56</b>
<b>Gd</b>	3.39	3.94	4.13	3.96	3.08	3.76	3.40	3.22	<b>3.61</b>	2.46	2.83	2.16	2.68	2.40	1.84	2.24	1.54	<b>2.27</b>
<b>Tb</b>	0.44	0.52	0.54	0.50	0.44	0.49	0.46	0.45	<b>0.48</b>	0.38	0.43	0.33	0.39	0.35	0.25	0.36	0.22	<b>0.34</b>
<b>Dy</b>	2.24	2.76	2.77	2.63	2.31	2.82	2.26	2.32	<b>2.51</b>	2.12	2.67	1.98	2.28	2.04	1.33	1.98	1.20	<b>1.95</b>
<b>Ho</b>	0.43	0.48	0.53	0.49	0.43	0.50	0.47	0.42	<b>0.47</b>	0.48	0.52	0.41	0.47	0.41	0.26	0.38	0.21	<b>0.39</b>
<b>Er</b>	1.17	1.27	1.50	1.38	1.24	1.32	1.25	1.23	<b>1.3</b>	1.34	1.62	1.26	1.47	1.25	0.86	1.19	0.62	<b>1.2</b>
<b>Tm</b>	0.17	0.19	0.22	0.20	0.16	0.18	0.19	0.18	<b>0.19</b>	0.23	0.25	0.22	0.23	0.19	0.12	0.19	0.10	<b>0.19</b>
<b>Yb</b>	1.17	1.28	1.36	1.24	1.16	1.27	1.29	1.16	<b>1.24</b>	1.57	1.82	1.41	1.58	1.40	0.76	1.24	0.71	<b>1.31</b>
<b>Lu</b>	0.17	0.18	0.19	0.21	0.17	0.18	0.19	0.19	<b>0.19</b>	0.24	0.30	0.24	0.25	0.22	0.14	0.19	0.12	<b>0.21</b>
<b>Σ REE</b>	110.18	116.27	134.72	125.70	104.81	118.01	115.30	107.55	<b>116.57</b>	113.00	129.04	98.99	110.87	109.14	77.97	86.58	80.00	<b>100.7</b>
<b>(La/Yb)<sub>n</sub></b>	11.32	11.04	13.54	12.82	11.54	12.14	12.16	12.12	<b>12.09</b>	11.64	11.31	12.14	11.35	12.91	16.80	11.12	18.37	<b>13.21</b>
<b>(La/Lu)<sub>n</sub></b>	11.91	11.99	14.80	11.57	12.03	13.09	12.62	11.31	<b>12.41</b>	11.63	10.48	10.90	10.96	12.55	13.94	11.09	16.61	<b>12.27</b>
<b>(La/Sm)<sub>n</sub></b>	2.72	2.71	3.43	3.08	2.99	3.27	3.42	3.22	<b>3.1</b>	5.60	5.33	6.12	5.28	5.67	5.39	4.86	5.45	<b>5.46</b>
<b>(Gd/Yb)<sub>n</sub></b>	2.34	2.49	2.46	2.58	2.15	2.40	2.13	2.25	<b>2.35</b>	1.27	1.26	1.24	1.37	1.39	1.96	1.46	1.75	<b>1.46</b>
<b>Eu/Eu*</b>	0.28	0.22	0.23	0.24	0.27	0.23	0.21	0.23	<b>0.24</b>	0.17	0.16	0.16	0.16	0.17	0.19	0.13	0.19	<b>0.17</b>
Sample	167	166	165	163	162	161	160	159	158	Avg.	108							
Lithology	Alkali riebeckite granite										Xenolith							
<b>La</b>	45.50	72.00	80.90	80.30	106.60	118.60	118.90	113.60	118.70	<b>95.01</b>	73.60							
<b>Ce</b>	116.50	157.70	168.10	157.60	217.20	236.60	236.10	228.60	237.00	<b>195.04</b>	110.00							
<b>Pr</b>	13.98	18.53	19.91	18.84	25.79	26.75	27.58	26.52	28.03	<b>22.88</b>	9.84							
<b>Nd</b>	56.30	68.90	71.20	70.50	97.10	98.70	102.20	100.00	107.80	<b>85.86</b>	32.10							
<b>Sm</b>	13.57	13.06	12.76	12.35	17.40	16.57	17.54	17.04	18.83	<b>15.46</b>	5.37							
<b>Eu</b>	0.81	1.20	1.63	1.60	1.56	1.56	1.62	1.50	1.69	<b>1.46</b>	1.29							
<b>Gd</b>	14.67	10.68	11.13	11.66	15.21	14.09	14.85	14.26	15.45	<b>13.56</b>	4.57							
<b>Tb</b>	2.59	1.81	1.71	1.81	2.30	2.07	2.23	2.18	2.12	<b>2.09</b>	0.63							
<b>Dy</b>	15.51	10.46	10.16	10.67	13.42	11.72	12.39	12.02	11.44	<b>11.98</b>	3.31							
<b>Ho</b>	3.28	2.24	2.03	2.09	2.68	2.32	2.41	2.47	2.24	<b>2.42</b>	0.70							

(Continued)

Table 2. (Continued)

Sample Lithology	167	166	165	163	162	161	160	159	158	Avg.	108 Xenolith
<b>Er</b>	9.65	6.84	6.04	6.27	7.97	6.54	6.75	6.98	6.43	<b>7.05</b>	2.12
<b>Tm</b>	1.39	1.05	0.93	0.96	1.15	1.00	0.98	0.98	0.94	<b>1.04</b>	0.35
<b>Yb</b>	8.93	7.22	6.26	6.45	7.54	6.38	6.86	6.65	6.35	<b>6.96</b>	2.58
<b>Lu</b>	1.36	1.13	0.98	1.02	1.18	1.01	1.08	1.00	1.04	<b>1.09</b>	0.50
<b>Σ REE</b>	304.04	372.82	393.74	382.12	517.10	543.91	551.49	533.80	558.06	<b>461.9</b>	246.96
<b>(La/Yb)<sub>n</sub></b>	3.46	6.77	8.78	8.46	9.60	12.63	11.77	11.60	12.70	<b>9.53</b>	19.38
<b>(La/Lu)<sub>n</sub></b>	3.47	6.61	8.57	8.17	9.38	12.19	11.43	11.79	11.85	<b>9.27</b>	15.28
<b>(La/Sm)<sub>n</sub></b>	2.09	3.44	3.96	4.06	3.83	4.47	4.23	4.16	3.94	<b>3.8</b>	8.56
<b>(Gd/Yb)<sub>n</sub></b>	1.33	1.20	1.44	1.46	1.63	1.79	1.75	1.73	1.97	<b>1.59</b>	1.43
<b>Eu/Eu*</b>	0.04	0.08	0.10	0.10	0.07	0.08	0.07	0.07	0.07	<b>0.08</b>	0.19

$$Eu/Eu^* = [Eu_n/(Sm_n + Gd_n)]/2.$$

calc-alkaline fields (Fig. 7c). The alkaline affinity of the individual granitic series is indicated by the diagram of Sylvester (1989) which is used for rocks with  $SiO_2 \geq 68$  wt % and discriminates between alkaline, calc-alkaline and highly fractionated calc-alkaline granites (Fig. 7d). In this diagram, two samples (# 132 and 118) of the granodiorite fall in the calc-alkaline field while the rest of the samples plot out of the diagram since they have  $SiO_2$  content less than 68 wt %. The monzogranite samples plot in the highly fractionated calc-alkaline granites field, and the alkali riebeckite granite samples plot in the alkaline field (Fig. 7d). According to the agpatic index ( $AI = Na + K/Al$ ) of Liégeois and Black (1987), the monzogranite and the granodiorite samples have average agpatic indices (AIs) of 0.86 and 0.58, respectively, and are thus classified as calc-alkaline granites. The agpatic index of the alkali riebeckite granites ( $AI = 1.01$ ) is in accordance with their alkaline affinity (Fig. 7e). On A/NK ( $A/NK = \text{molar ratio } (Al_2O_3/(Na_2O + K_2O))$ ) versus alumina saturation index (ASI) diagram (Zen, 1986), the granodiorite and the alkali riebeckite granite are metaluminous while the monzogranite samples plot at the boundary between the metaluminous and the peraluminous domains (Fig. 7f).

The studied samples are characterized by a left-inclined mantle-normalized diagram caused by the enrichment of both Pb and large-ion lithophile elements (LILEs) such as Rb, Th and U, along with depletion in the high-field strength elements (HFSEs) (Fig. 8a). The mantle-normalized spider diagram of the granodiorite is characterized by deep Nb–Ta negative anomalies and moderate to weak negative P and Ti anomalies (Fig. 8a). On the other hand, the monzogranite pattern is characterized by strong negative P anomalies and moderate Ti, Nb and Ba negative anomalies (Fig. 8a). Lastly, the multi-elements pattern of the alkali riebeckite granite is characterized by strong depletion in Sr, P and Ti concentrations and moderate depletion of Ba concentration (Fig. 8a).

#### 4.b.2. Rare earth elements

The chondrite-normalized REE patterns of the three granite rock types (Fig. 8b) are characterized by higher light rare earth elements (LREE) abundances (average  $(La/Sm)_n = 3.10$  for granodiorite, 5.46 for monzogranite and 3.80 for alkali riebeckite granite) than for the heavy rare earth elements (HREE) (average  $(Gd/Yb)_n = 2.35$  for granodiorite, 1.46 for monzogranite and 1.59 for alkali riebeckite granite) (Fig. 8b; Table 2). The granodiorite is characterized by a smooth pattern with no Eu anomaly (Fig. 8b; Table 2). On the other hand, the monzogranite REE pattern shows a steeper slope compared to granodiorite and alkali riebeckite granite ( $(La/Yb)_n = 13.21, 12.09$  and  $9.53$ , on average, respectively) (Fig. 8b). The alkali riebeckite granite pattern displays a stronger negative Eu anomaly than the monzogranite (average  $(Eu/Eu^*) = 0.08, 0.17$ , respectively) (Fig. 8b). The alkali riebeckite granite samples have higher total REE contents than the granodiorite and the monzogranite samples (average  $\Sigma REE = 461.90$  ppm, 116.58 ppm and 100.70 ppm, respectively).

## 5. Discussion

### 5.a. Granite types and tectonic environment

The granodiorite of the Abu Kharif area has petrological and geochemical characteristics of typical I-type granites (according to I-type described by Chappell & White, 1974; White & Chappell, 1983; Whalen *et al.* 1987). However, the monzogranite

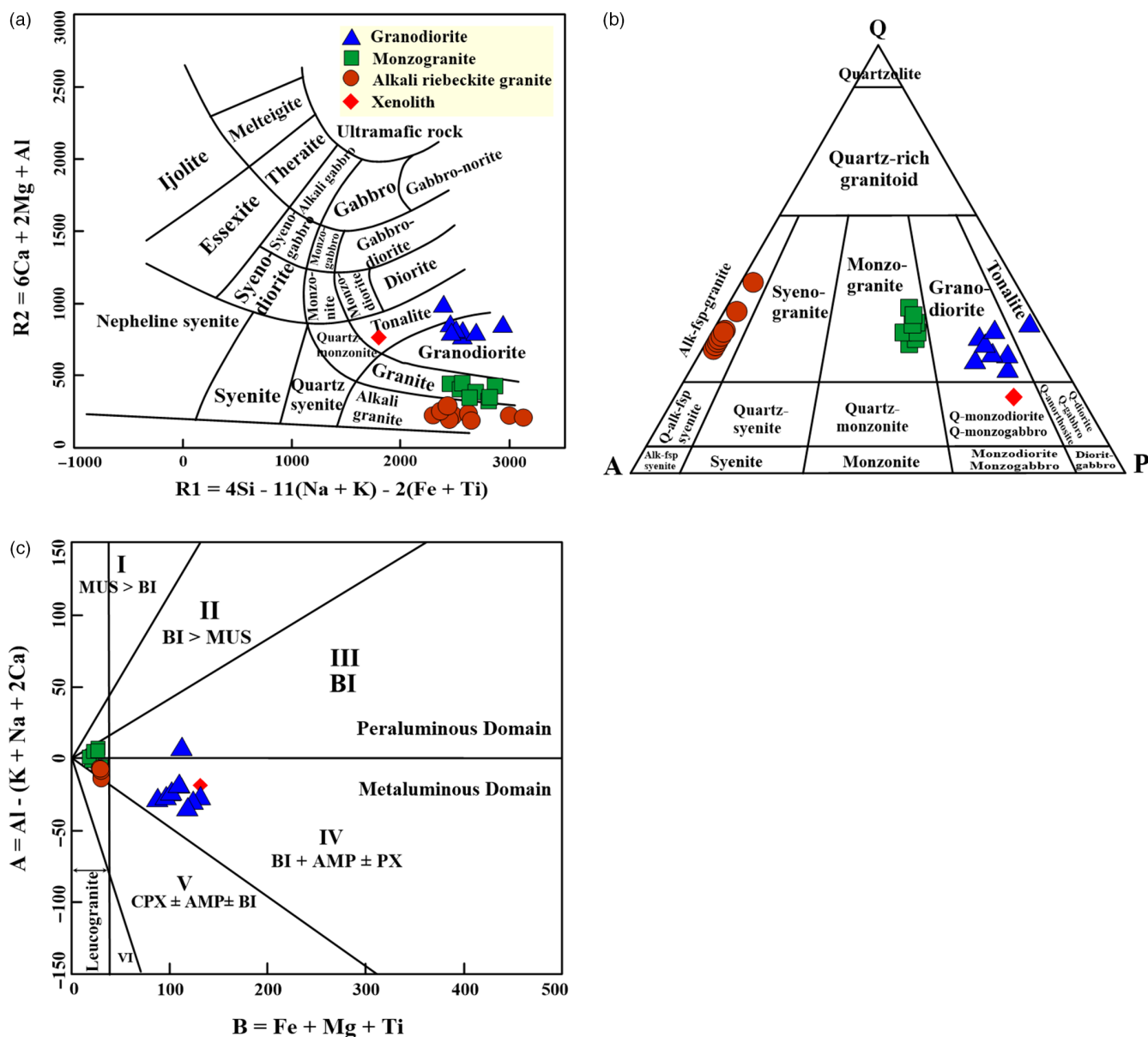


**Fig. 5.** (Colour online) Geochemical classification of studied granite rock types. (a) The classification of the studied granite rock types using the parameters  $R_1$ - $R_2$  (De La Roche *et al.* 1980). (b) The QAP diagram (Streckeisen, 1976) showing the studied granite rock types according to their CIPW normative mineral compositions. Q = quartz, A = alkali feldspar and P = plagioclase feldspar, Alk-fsp-granite = alkali feldspar granite. (c) A-B multicatic diagram (Debon & Le Fort, 1983). Each of the six sectors, I-VI, corresponds to a specific mineral composition. MUS = muscovite, BI = biotite, AMP = amphibole, PX = pyroxene and CPX = clinopyroxene.

and alkali riebeckite granite share some significant similarities to highly fractionated I-type and/or A-type granites. Both are characterized by high contents of  $SiO_2$ , alkalis, Fe#, Rb, Nb and Y and low contents of MgO and CaO (Tables 1, 2). Nevertheless, the monzogranite plots entirely in the field of highly fractionated I-type granites defined by Sylvester (1989) and Whalen *et al.* (1987) (Figs. 7, 9a, respectively). On the other hand, the alkali riebeckite granite samples plot entirely in the field of A-type granite (Fig. 9b). Eby (1990, 1992) subdivided the A-type magmas into two groups: A1, which represents differentiates of mantle-derived oceanic island basalts (anorogenic or rift zone magmas), and A2, which represents mainly crustal magmas of post-orogenic to anorogenic setting.

On the primitive-mantle-normalized diagram (Fig. 8a), the granodiorite is characterized by enrichment of LILE relative to

HFSE and negative Ta-Nb anomaly; these features were ascribed to volcanic arc granite (Pearce *et al.* 1984) formed by subduction-related processes (Saunders *et al.* 1980). Moreover, the low  $TiO_2$  concentration (<1 wt %) is consistent with volcanic-arc granite (Green, 1980). However, the monzogranite has higher Ta/Zr and Ta/Hf ratios (0.01 and 0.3, on average, respectively) than those of volcanic-arc intrusions (Harris *et al.* 1986) as well as slightly higher K, Rb, Ba and Sr contents approaching those of collision granites from the Eastern Desert of Egypt (e.g. Moghazi, 2002). The alkali riebeckite granite has  $Y/Nb < 1.2$  (A1-subtype), suggesting its anorogenic environment (Eby, 1992). The high Fe# (0.99-1.00) for the alkali riebeckite granite is also typical of an anorogenic-related regime (Anderson & Cullers, 1978). Moreover, the alkali riebeckite granite is characterized by high  $K_2O$ , Th, Nb, Ta and low Ba, Sr, Ti and Eu concentrations, similar

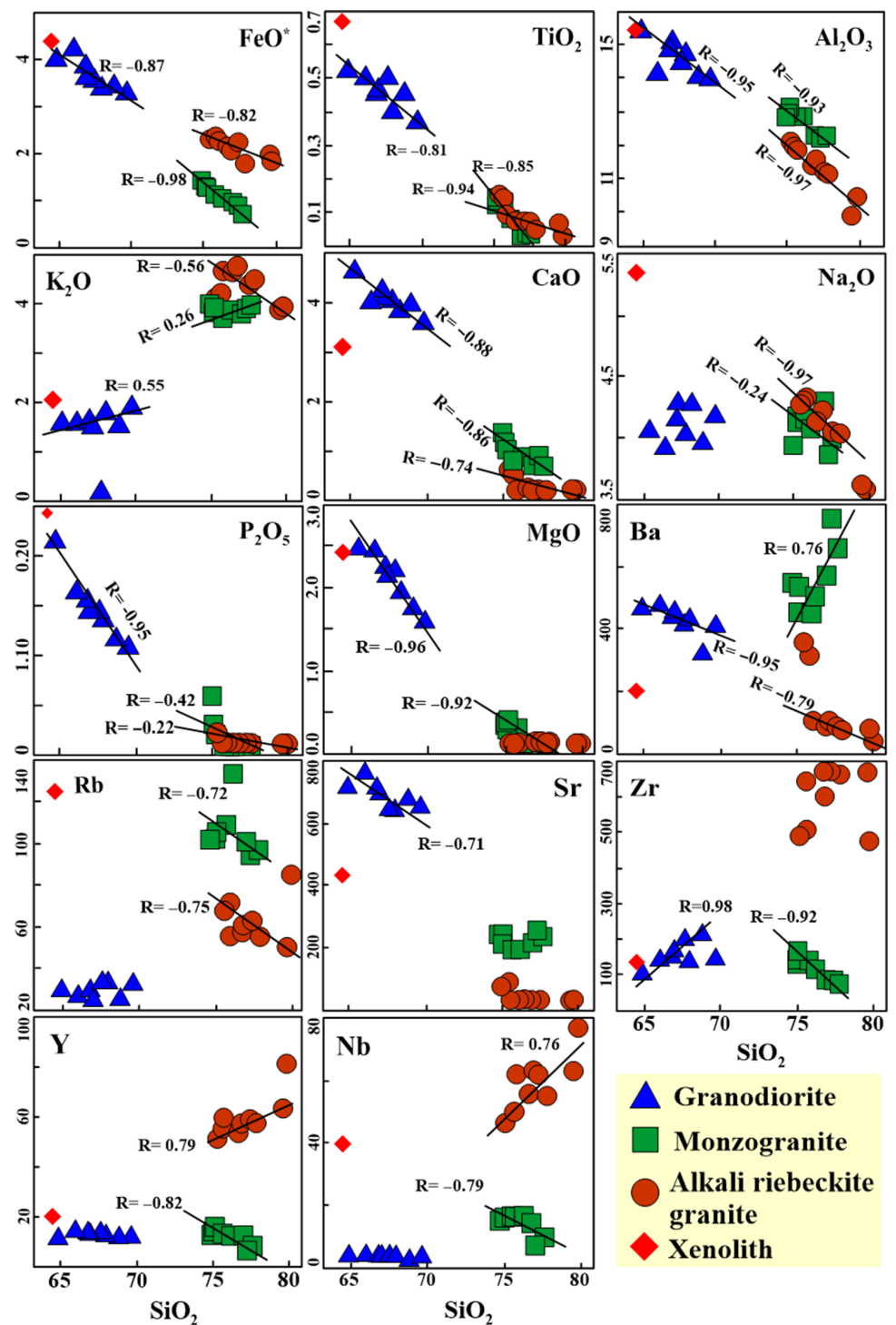


**Fig. 6.** (Colour online) Major- and trace-element Harker diagrams for the studied granodiorite, monzogranite and alkali riebeckite granite in the Abu Kharif area.

to those of anorogenic rift-related granite (Harris *et al.* 1986; Pearce, 1996). The tectonic setting discrimination between the three studied granite intrusions is supported by further diagrams of Rb vs Y + Nb (Fig. 9c) and Rb–Ta–Hf (Fig. 9d). Additionally, Agrawal (1995) suggested multivariate discriminant analyses, using major-elements composition to distinguish between anorogenic and orogenic granites as well as the orogeny subclasses late-orogenic and post-orogenic. The discriminant rules proposed by Agrawal (1995) show that the granodiorite and the monzogranite are of orogenic nature ( $DC_1$  is a positive quantity). The

granodiorite is further classified as late-orogenic ( $DC_2$  is a positive quantity) and the monzogranite as post-orogenic ( $DC_2$  is a negative quantity). On the other hand, the alkali riebeckite granite is of anorogenic nature ( $DC_1$  is a negative value) (Table 1).

### 5.b. Petrogenesis of the magmatic units

The genetic relationship between different types of Pan-African Egyptian granites still remains a matter of debate. Many geochemical observations indicate that the Abu Kharif granite rocks were emplaced from different magma types in different tectonic settings.

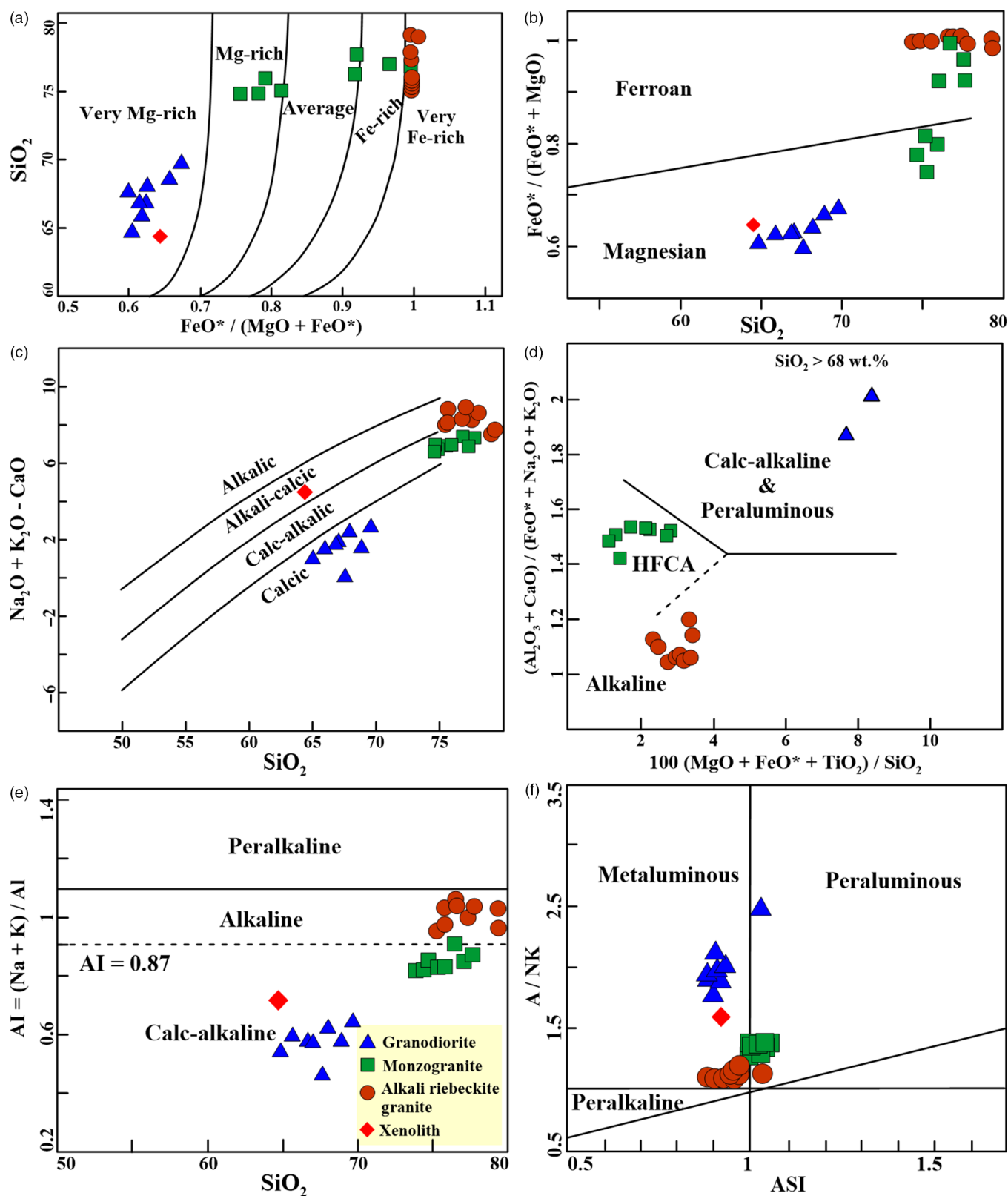


**Fig. 7.** (Colour online) (a)  $\text{SiO}_2$  versus  $\text{FeO}^*/(\text{MgO} + \text{FeO}^*)$  classification diagram (Dewitt, 1989). (b)  $\text{FeO}^*/(\text{FeO}^* + \text{MgO})$  versus  $\text{SiO}_2$  diagram (Frost *et al.* 2001). The dividing line is after Frost and Frost (2008). (c)  $(\text{Na}_2\text{O} + \text{K}_2\text{O} - \text{CaO})$  versus  $\text{SiO}_2$  diagram (Frost & Frost, 2008). (d)  $(\text{Al}_2\text{O}_3 + \text{CaO})/(\text{FeO}^* + \text{Na}_2\text{O} + \text{K}_2\text{O})$  versus  $100(\text{MgO} + \text{FeO}^* + \text{TiO}_2)/\text{SiO}_2$  diagram (Sylvester, 1989). HFCA = highly fractionated calc-alkaline granites. (e) Agpatic index (AI) vs  $\text{SiO}_2$  diagram. The dashed line with  $\text{AI} = 0.87$  (Liégeois & Black, 1987) separates alkaline and calc-alkaline series. (f) Molar  $\text{Al}_2\text{O}_3/(\text{Na}_2\text{O} + \text{K}_2\text{O})$  (A/NK) vs alumina saturation index (ASI) ( $\text{ASI} = \text{Al}_2\text{O}_3/(\text{Na}_2\text{O} + \text{K}_2\text{O} + \text{CaO})$ ) (Zen, 1986).

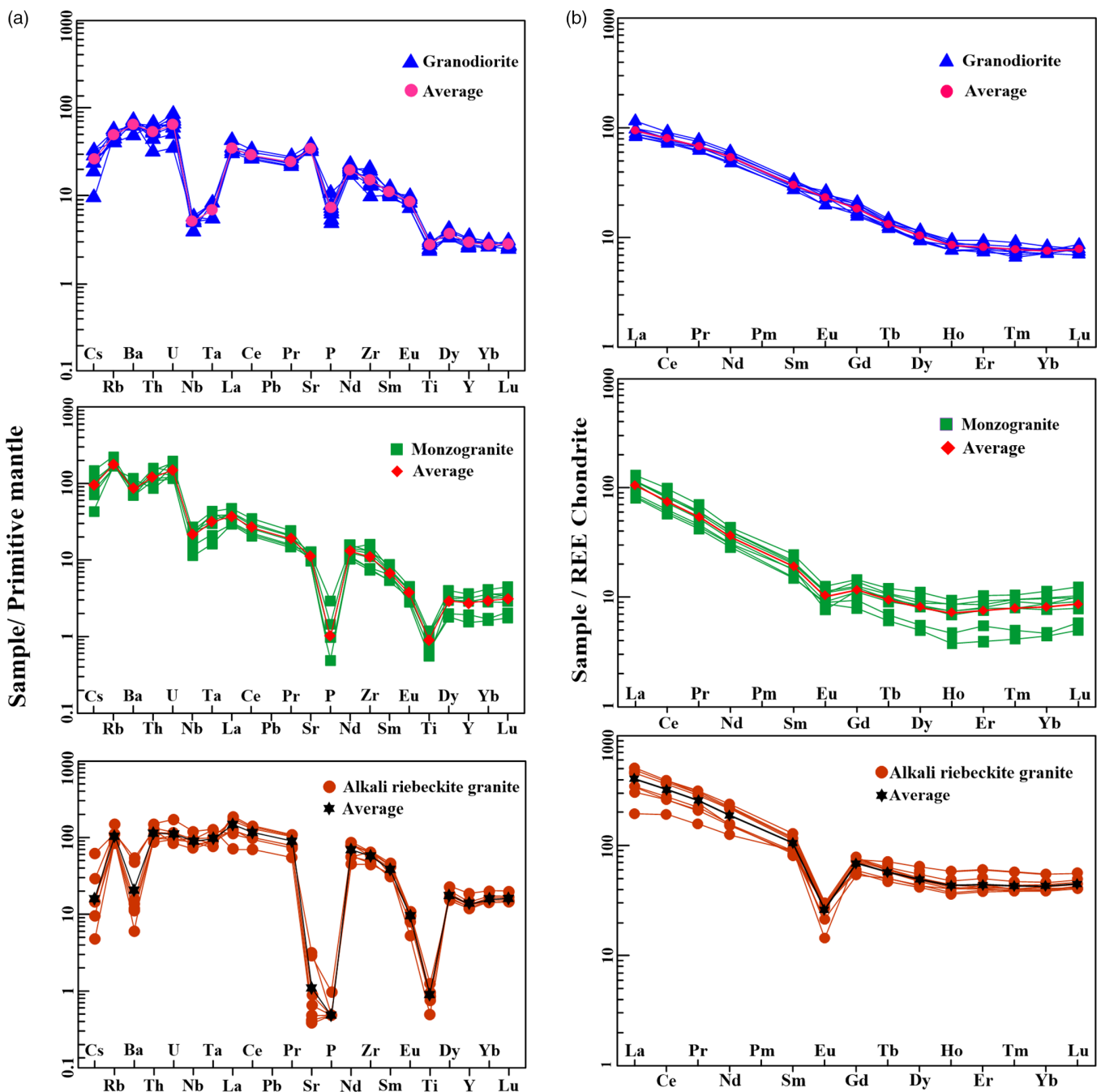


**Fig. 8.** (Colour online) (a) Primitive-mantle-normalized trace-element spider diagrams for the Abu Kharif granodiorite, monzogranite and alkali riebeckite granite. Chondrite-normalizing factors are from McDonough and Sun (1995). (b) REE patterns for the Abu Kharif granite rock types. Normalization values are after McDonough and Sun (1995).

Major- and trace-element variation diagrams define the Ediacaran monzogranite and Cambrian alkali riebeckite granite as not representing the fractionation end-member of the Cryogenian granodiorite, where samples from the granite rock types show consistent trends, but with a compositional gap (Fig. 6). Such geochemical variations may indicate that magmatic types in the Abu Kharif area are not genetically related. Variation diagrams of K/Rb vs Rb and  $\text{CaO}/\text{Al}_2\text{O}_3$  vs Mg# do not show colinear variation between the studied granite types (Fig. 10a, b). The variation in value of Zr/Nb ratio between the granodiorite, monzogranite and alkali riebeckite granite (47.12, 8.57 and 10.29, on average, respectively), where both Zr and Nb are strongly incompatible

elements in alkaline magmas (McDonald *et al.* 1987), indicates that these rock types are evolved from different magma sources. In addition, the chondrite-normalized REE patterns for the studied intrusions show that the granodiorite pattern displays a general decrease in concentrations from La to Lu without Eu anomalies. On the other hand, the monzogranite and alkali riebeckite granite have a conspicuous fractionated pattern with flat HREE and a marked negative Eu anomaly (Fig. 8b).

The tectonic settings of the granite intrusions in the Abu Kharif area are late-orogenic, post-orogenic and anorogenic for the granodiorite, monzogranite and alkali riebeckite granite, respectively, according to geochemical characteristics (Fig. 9c, d; Table 2).

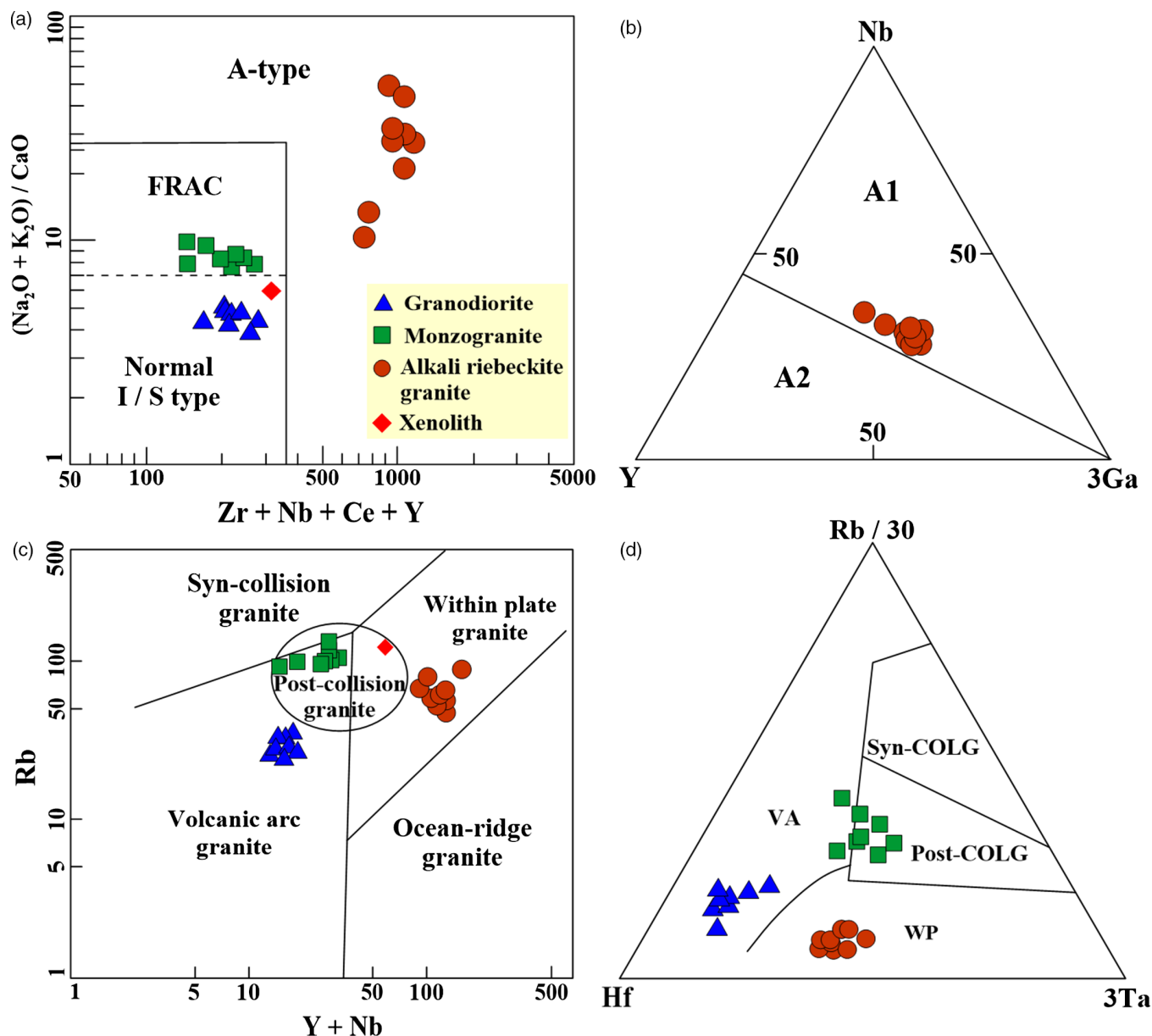


**Fig. 9.** (Colour online) Granite type and tectonic discrimination diagrams for the studied samples of Abu Kharif granite rocks. (a)  $(\text{Na}_2\text{O} + \text{K}_2\text{O})/\text{CaO}$  versus  $\text{Zr} + \text{Nb} + \text{Ce} + \text{Y}$  discrimination diagram (Whalen *et al.* 1987). FRAC = fractionated I-type granites. (b)  $\text{Y}-\text{Nb}-3\text{Ga}$  (ppm) A-type granite discrimination ternary diagram (Eby, 1992) showing the A1 nature of the studied alkali riebeckite granite. (c)  $\text{Y} + \text{Nb}$  versus  $\text{Rb}$  plot (Pearce *et al.* 1984). The middle ellipse marks post-collision granites after Pearce (1996). (d) Ternary  $\text{Rb}-\text{Hf}-\text{Ta}$  diagram (Harris *et al.* 1986) for the Abu Kharif granitoid rocks. Syn-COLG (syn-collision granite); VA (volcanic arc granite); WP (within-plate granite); Post-COLG (post-collision granite).

The anorogenic alkali riebeckite granite points to an emplacement into Pan-African crust following the Pan-African orogenic cycle (Abdel-Rahman & El-Kibbi, 2001; Abdel-Rahman, 2006).

Since the studied Abu Kharif magmatic units display metaluminous to slightly peraluminous affinities and have low normative corundum contents (<1%), they have not been formed by partial melting of metapelitic source which would lead to strongly peraluminous magmas (Jung *et al.* 1998). Likewise, the  $\text{TiO}_2/\text{Zr}$  ratios of the studied granite rock types vary little compared to those of potential metasedimentary origin (Garcia *et al.* 1994).

### 5.b.1. Origin of the granodiorite

Several genetic models have been proposed to discuss and explain the origin, source and development of granite rocks in the Nubian

Shield. These models suggest that the I-type Cryogenian granodiorite was generated through either fractionation from mantle-derived magmas in subduction settings, or from melting of lower mafic crust (El-Sayed, 1998; Furnes *et al.* 1996; El-Shazly & El-Sayed, 2000; El-Sayed *et al.* 2001). In the Eastern Desert of Egypt, the I-type granodiorite rocks are chronocorrelated with the mantle-derived metagabbro-diorite complexes of the island-arc stage, which are frequently considered as their magmatic precursor (El-Sayed, 2003; Basta *et al.* 2017).

Several lines of evidence argue against the hypothesis that the investigated granodiorite rocks were produced by extensive fractional crystallization of a mantle-derived mafic magma, represented by the island-arc metagabbros in the Eastern Desert (~850–750 Ma; Furnes *et al.* 1996). These evidences include: (1)

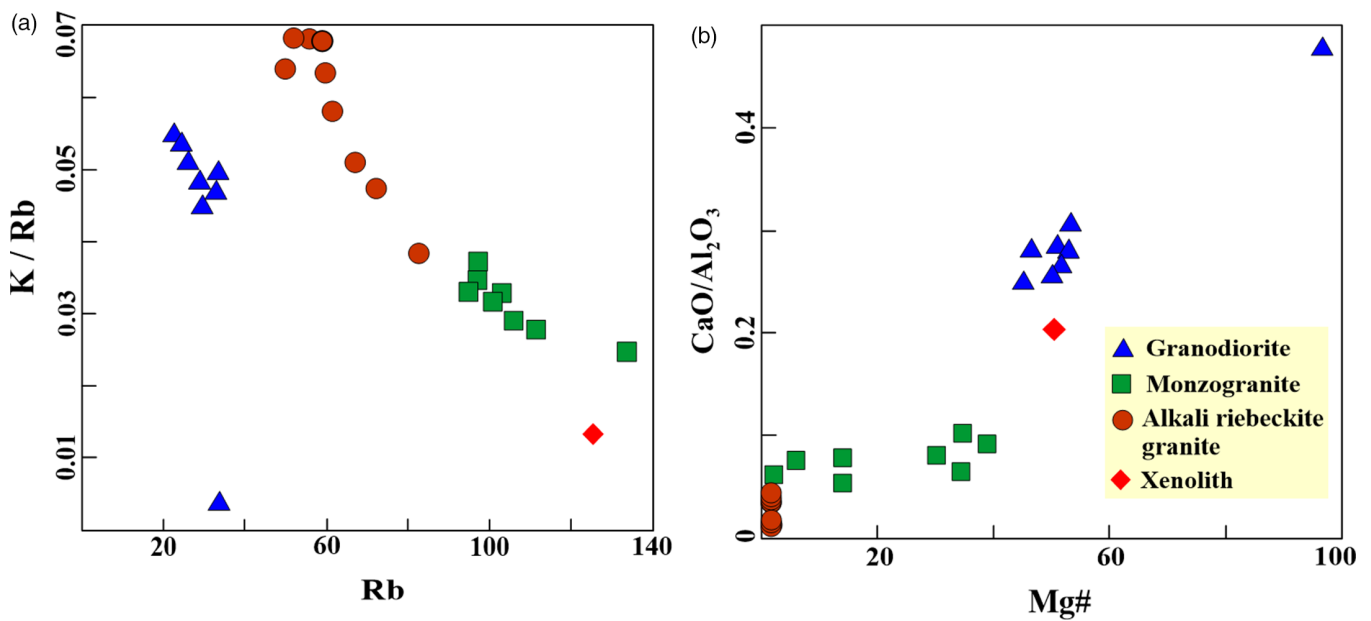


**Fig. 10.** (Colour online) (a) Rb versus K/Rb variation diagram for the studied granite rock types. (b) CaO/Al<sub>2</sub>O<sub>3</sub> versus Mg# variation diagram for the studied granite rock types.

high Sr, CaO and Ba abundances (687 ppm, 4.09 wt % and 426 ppm, on average, respectively) and the lack of a significant Eu anomaly require a high percentage of melting and the elimination of all or most of the feldspar by melting; (2) granite melts derived from the extreme fractional crystallization of a gabbroic magma are characterized by strong enrichment in many HFSE (Turner *et al.* 1992), which is not the case for the investigated granodiorites (Fig. 8a); (3) the absence of a collinear trend between the gabbro–diorite complex and the investigated granodiorite argue against its relation to the gabbro–diorite complex through fractional crystallization (Fig. 11a); and (4) in the Abu Kharif area, I-type granodiorite in large volumes is associated with only minor metagabbro–diorite rocks.

The generation of Abu Kharif granodiorite by partial melting of lower crustal rocks seems to be a more feasible hypothesis. The molar CaO/(MgO + FeO\*) versus Al<sub>2</sub>O<sub>3</sub>/(MgO + FeO\*) diagram (Altherr *et al.* 2000) indicates that the granodiorite could be derived by melting of a mafic source (Fig. 11b). The granodiorite hosts amphibolitic xenoliths, zoned and twinned core plagioclase crystals and poikilitic biotite crystals. These features may reflect that batch partial melting of a basic source played an important role in the genesis of the granodiorite. Thus, the amphibolitic xenoliths can be considered as restites (refractory residues) remaining after high degrees of partial melting of an amphibolitic source.

In order to test our model regarding the generation of the investigated granodiorite via partial melting of lower amphibolitic crustal source, we used the non-model batch partial melting equation of Shaw (1970):  $C_L = C_0/[D_0 + F(1-P)]$ , where  $C_L$  is the concentration of the trace element in the melt,  $C_0$  the concentration in the source,  $F$  the melt fraction,  $D_0$  the bulk distribution coefficient for the starting assemblage, and  $P$  is the bulk distribution coefficient of the minerals that make up the melt. The results of Rb, Ba, Sr, Nd, Ba, Zr, Nb, Y, Ce, Yb and Sm batch partial melting modelling of mafic source using the average content of the amphibolitic rocks (Furnes *et al.* 1996) are presented in Table 3. The results indicate a close match between the modelled trace elements by ~75 %

melting of amphibolitic source and those in the least evolved granodiorite sample (# 121) (Table 3; Fig. 11c).

Although the quantitative trace-elements batch melting model can explain most of the chemical variation in the granodiorite, there are some geochemical characteristics suggesting that fractional crystallization may have played a role in the evolution of the granodiorite (Fig. 8a). The low content of Nb, Zr and Y (3 ppm, 156 ppm and 13 ppm, on average, respectively) suggests that the fractionation of accessory minerals contributes to the evolution of the granodiorite. Negative Ti anomalies reflect the fractionation of Ti-bearing minerals (Wang *et al.* 2014) while negative P anomalies should result from apatite and/or monazite crystallization. Negative Nb and Ta result from rutile separation (Foley *et al.* 2000).

Major-elements geochemical modelling software of Wright and Doherty (1970) was used to constrain the proposed role of the fractional crystallization hypothesis. The results of the calculations and the compositions of the fractionating minerals are given in Table 4. The results show that the most evolved sample of the granodiorite (sample# 132) could be produced by 11 % fractional crystallization of the least evolved sample (sample# 121). The fractionated phases are 5.19 % hornblende, 5.05 % biotite, 0.39 % apatite and 0.14 % titanite (Table 4). Thus, the granodiorite was generated by ~75 % batch partial melting of amphibolitic source followed by fractional crystallization of hornblende, biotite, apatite and titanite.

### 5.b.2. Origin of the monzogranite

The post-orogenic highly fractionated monzogranite is characterized by hosting xenoliths of dioritic composition. The dioritic xenoliths display lower SiO<sub>2</sub> (64.5 wt %) and higher Al<sub>2</sub>O<sub>3</sub> (15.36 wt %), MgO (2.41 wt %), FeO\* (4.33 wt %) and TiO<sub>2</sub> (0.77 wt %) than those of the host monzogranites (Table 1). These features indicate calc-alkaline affinity for the dioritic xenoliths (Juan & Xin, 2009).

The lack of disequilibrium textures such as patchy zoned plagioclase and pyroxene cores in hornblende and absence of acicular apatite preclude a genetic relation of the monzogranite and the



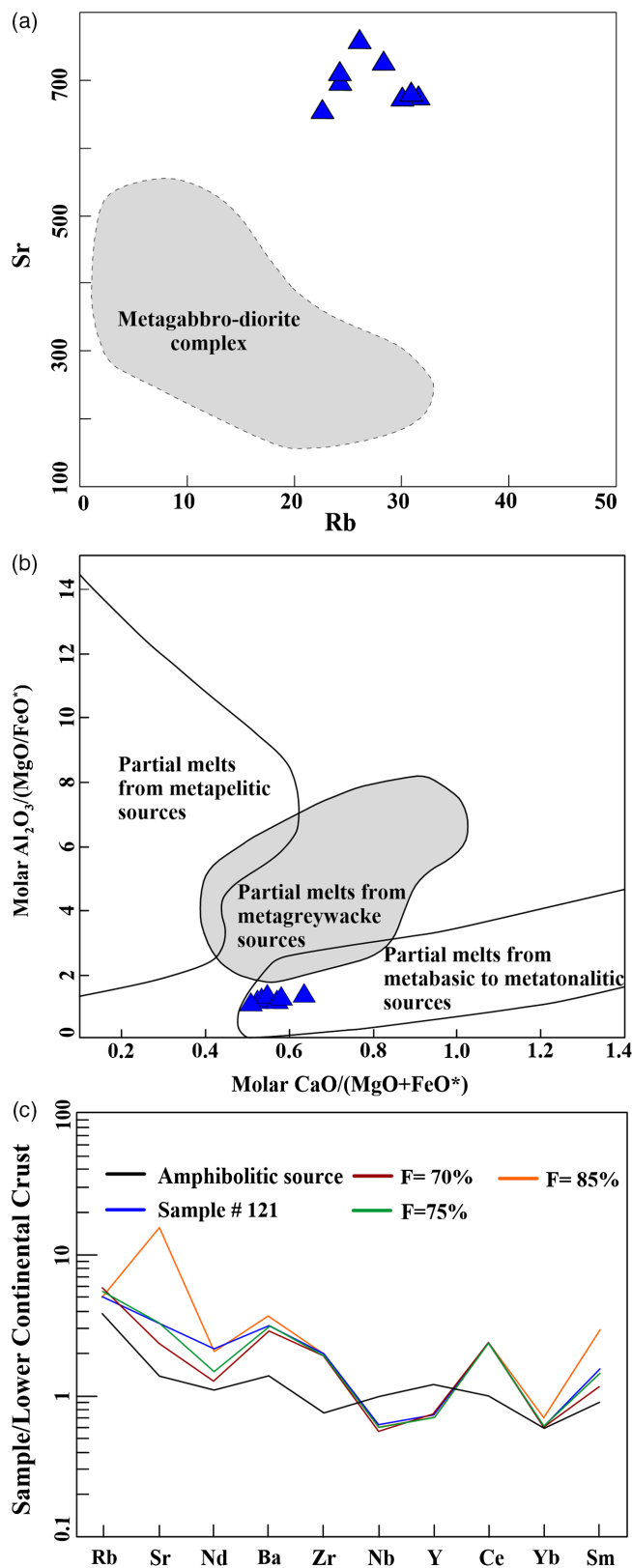


**Fig. 11.** (Colour online) (a) Rb versus Sr diagram of the granodiorite rocks in the Abu Kharif area. The field of the gabbro–diorite complex is from El-Sayed (2003). (b) Molar  $Al_2O_3/(MgO + FeO^*)$  versus molar  $CaO/(MgO + FeO^*)$  diagram (Altherr *et al.* 2000). Outlined fields denote compositions of partial melts obtained in experimental studies by dehydration melting of various bulk compositions (Wolf & Wyllie, 1994; Douce & Beard, 1995, 1996; Gardien *et al.* 1995; Douce, 1996; Singh & Johannes, 1996; Thompson, 1996; Douce & McCarthy, 1998). (c) Trace-element modelling for the granodiorite. The compositions of melt derived by 70 %, 75 % and 85 % melting of average amphibolitic source to produce the least evolved granodiorite (sample# 121) are shown. Normalization values of lower continental crust are after Taylor and McLennan (1995). Symbols as Figure 10.

**Table 3.** Results of trace-element non-modal partial melting modelling for different degrees of amphibolitic source melting

	Source (amphibolite)	D <sub>0</sub>	P	Calculated melt			Observed melt
				F = 70 %	F = 75 %	F = 85 %	
<b>Rb</b>	20.00	0.25	0.44	31.02	29.72	27.42	26.60
<b>Sr</b>	319.00	2.93	4.34	540.13	753.25	3572.23	760.00
<b>Nd</b>	14.00	2.36	3.15	16.37	18.73	26.29	27.70
<b>Ba</b>	210.00	0.97	1.70	437.50	471.91	560.00	473.00
<b>Zr</b>	54.00	0.43	1.05	136.71	137.58	139.35	137.70
<b>Nb</b>	6.00	2.31	1.84	3.48	3.57	3.76	3.80
<b>Y</b>	23.00	1.24	0.40	13.87	13.63	13.16	14.30
<b>Ce</b>	23.00	0.38	0.95	55.42	55.09	54.44	55.40
<b>Yb</b>	1.30	0.163	1.91	1.31	1.37	1.52	1.36
<b>Sm</b>	2.90	2.89	4.04	3.79	4.73	9.35	4.94

Amphibolite composition is after Furnes *et al.* (1996). Observed melt = compositions of the least evolved sample of the granodiorite (sample# 121). The distribution coefficients used are after GERM (Geochemical Earth Reference Model; <http://www.earthref.org/GERM>). D<sub>0</sub> = bulk distribution coefficient for the starting assemblage; P = bulk distribution coefficient of the minerals that make up the melt; F = melt fraction.

**Table 4.** Results of fractionation modelling for the granodiorite based on the method of Wright and Doherty (1970)

Fractionation of granodiorite (from sample# 121 to sample# 132)							
Fractionation phases							
	Hornblende	Biotite	Titanite	Apatite	Observed daughter	Observed parent	Calculated parent
<b>SiO<sub>2</sub></b>	47.99	36.3	28.82	0.00	69.63	65.99	67.63
<b>TiO<sub>2</sub></b>	0.68	1.76	33.75	0.00	0.47	0.60	0.61
<b>Al<sub>2</sub>O<sub>3</sub></b>	6.15	16.11	1.75	0.00	13.98	14.13	13.93
<b>FeO*</b>	13.83	23.05	2.00	0.19	3.28	4.64	4.77
<b>MnO</b>	0.39	0.81	0.09	1.52	0.01	0.01	0.07
<b>MgO</b>	12.98	6.39	0.09	0.54	1.59	2.56	2.52
<b>CaO</b>	11.08	0.03	25.94	52.4	3.58	4.06	4.08
<b>Na<sub>2</sub>O</b>	0.93	0.00	0.25	0.00	4.20	3.91	3.86
<b>K<sub>2</sub>O</b>	0.47	8.56	0.00	0.00	1.94	1.61	2.78
<b>P<sub>2</sub>O<sub>5</sub></b>	0.00	0.00	0.00	40.98	0.10	0.16	0.26

Parent (sample# 121) = 88.6 % daughter (sample# 132) + 5.19 % hornblende + 5.05 % biotite + 0.39 % apatite + 0.14 % titanite.

Fractionating phases (10.77 %): 48.19 % hornblende, 46.89 % biotite, 3.6 % apatite and 1.3 % titanite.

R<sup>2</sup> = 1.7.

The compositions of the used fractionating phases hornblende and biotite are after MM El-Sayed (unpub. PhD thesis, Alexandria Univ., 1994), while the compositions of titanite and apatite are after Deer *et al.* (1978). R<sup>2</sup>: sum of squares of the residual.

captured xenoliths through a mingling–mixing process (El-Sayed, 2003). In the Harker diagrams, the major and trace elements of the xenolith plotted off the linear trend with their host monzogranite (Fig. 6), which precludes neither fractional crystallization nor mixing as a mafic–felsic magma evolution process. These features may suggest that the dioritic xenoliths are rocks dragged during ascent of the magma to crustal levels.

The highly evolved composition of the monzogranite and absence of any basic rocks associated with it argue against its generation by fractional crystallization from a parental mafic magma. Based on petrological and geochemical data, the most acceptable mechanism for the origin of the monzogranite is crustal anatexis. For the Arabian Nubian Shield, two types of Pan-African crusts are proposed by Abdel-Rahman and Martin (1990), namely non-metasomatized and metasomatized calc-alkaline granitic rocks. The REE pattern of the calculated melt produced by 62 % batch

partial melting of normal ‘non-metasomatized’ Pan-African calc-alkaline granitic rocks (Abdel-Rahman, 2006) is consistent and matches the REE pattern of the studied highly fractionated monzogranite (Fig. 12).

The chemical data show that the monzogranite is evolved in composition, with SiO<sub>2</sub> contents ranging from 74.96 wt % to 77.59 wt %, and exhibits a narrow compositional range (Table 1). The overall trends of major and trace elements of the monzogranite in the variation diagrams (Fig. 6) as well as the fractionated nature of its REE ((La/Lu)<sub>n</sub> = 12.27, on average) (Table 2) suggest that the magma has undergone a minor degree of internal differentiation. The monzogranite samples exhibit K/Rb ratios >160 (306, on average), indicating that a fractional crystallization process could have played a role in the genesis of the monzogranite (Shaw, 1968). The low content of MgO (0.19 wt %), Fe<sub>2</sub>O<sub>3</sub>\* (1.21 wt %), P<sub>2</sub>O<sub>5</sub> (0.02 wt %) and depletion in Nb (17 ppm), Ta (1.39 ppm),

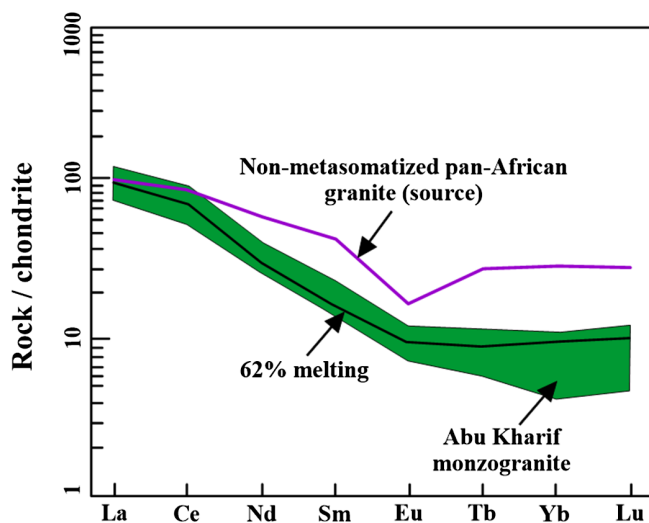


**Fig. 12.** (Colour online) Chondrite-normalized diagram showing the calculated REE patterns for melts produced by 62 % batch partial melting of non-metasomatized Pan-African calc-alkaline granitic rocks. The REE composition of the source materials and their modal proportions are after Abdel-Rahman and El-Kibbi (2001). Shaded green pattern represents the REE field of the studied monzogranite. Normalization values are taken from Taylor and McLennan (1985).

TiO<sub>2</sub> (0.18 wt %) and Eu (0.56 ppm) indicate the same. The strong P depletion suggests fractionation of apatite. Negative Nb–Ti anomalies are considered to be related to the separation of Ti-bearing phases. Strong Eu depletion requires extensive fractionation of plagioclase and/or K-feldspar. The investigated monzogranite displays negative Eu anomalies and is associated with negative Ba anomalies (Fig. 8a, b), which implies that the fractionation of the K-feldspar has the main role in this respect (Wilson, 2007).

Conventional, least-squares mixing major-elements geochemical modelling software of Wright and Doherty (1970) can be used to test the role of the fractional crystallization process in the genesis of the monzogranite. The calculations show that the most evolved sample of the monzogranite (sample# 115) can be formed by 12 % fractional crystallization from the least-evolved sample (sample# 110) through crystallization of plagioclase (6.12 %), biotite (2.33 %), K-feldspar (2.39 %), magnetite (0.88 %) and ilmenite (0.11 %) (Table 5). Thus, the monzogranite was formed by 62 % batch partial melting of the normal (non-metasomatized) Pan-African crust of calc-alkaline granite composition followed by a minor role of crystallization of plagioclase, biotite, K-feldspar, magnetite, ilmenite, apatite and titanite.

### 5.b.3. Origin of the alkali riebeckite granite

Several models have been proposed for the genesis of the A-type anorogenic granites. These models include (1) fractional crystallization from mantle-derived basaltic magmas (Turner *et al.* 1992; Moghazi, 1999; Mushkin *et al.* 2003; Frost & Frost, 2010); (2) partial melting of lower crustal materials followed by fractional crystallization (Küster & Harms, 1998; Jarrar *et al.* 2003; Abdel-Rahman, 2006); (3) contamination of mafic mantle-derived melt by lower crustal components in an extensional environment (Frost *et al.* 2002; Wu *et al.* 2002); and (4) assimilation and magma mixing between anatectic crustal and mantle-derived mafic magmas (Yang *et al.* 2006; Barboni & Bussy, 2013; Gao *et al.* 2016).

The alkali riebeckite granite of the Abu Kharif area is characterized by the absence of xenoliths, sharp intrusive contacts with

country rocks and absence of metasomatic effects, and homogeneous petrographic and geochemical nature. These features argue against the assimilation and magma-mixing hypothesis. The low Y/Nb (0.99, on average) and Yb/Ta (2.00, on average) ratios do not favour crustal contamination, which would have influenced these ratios (Wilson, 2007). The enriched unfractionated HREE pattern of the alkali riebeckite granite is inconsistent with batch melting of mantle-derived source (Stern & Gottfried, 1986) and suggests a garnet-free source (Wilson, 2007). The high Rb/Sr (4.77, on average) ratio with high Y (58.97 ppm, on average) and HREE is incompatible with partial melting of lower crustal materials.

Fluid influx may have caused metasomatism of the Pan-African crust, possibly by a Na–F-rich fluid phase (Abdel-Rahman, 2006). The volatile flux has catalysed the anatectic reactions near the base of the crust (Bailey, 1974). Abdel-Rahman (2006) proposed that the Abu Kharif alkali riebeckite granite was formed by partial melting of metasomatized Pan-African crustal granitic rocks. The REE pattern of the study Abu Kharif alkali riebeckite granite is similar to the REE pattern of calculated liquid produced by 65 % non-modal batch melting of metasomatized Pan-African calc-alkaline granites (Fig. 13a; Table 6).

However, the high differentiation index (95.17), Rb (63 ppm), Nb (60 ppm), Y (59 ppm) and K/Rb ratio (586) and low Eu (1.46 ppm), Ba (136 ppm), Sr (22 ppm), CaO (0.23 wt %) and MgO (0.01 wt %) concentrations of the alkali riebeckite granite require fractional crystallization of magmatic liquid (Turner *et al.* 1992; Mao *et al.* 2014) as well as reflecting the role of the source composition (Clemens & Stevens, 2012). The pronounced negative Eu, Sr and Ba anomalies in the chondrite-normalized and mantle-normalized diagrams (Fig. 8a, b) suggest that both plagioclase and K-feldspar fractionation played a major role in the genesis of the alkali riebeckite granite. Although the negative Eu anomaly was controlled by fractional crystallization of plagioclase, fractional crystallization of alkali feldspar seems more effective in controlling Ba abundances than that of plagioclase (Fig. 13b). The predominance of Na<sub>2</sub>O over K<sub>2</sub>O in the alkali riebeckite granite (Table 1) suggests fractionation of K-rich feldspar. In addition, the significant negative Ba, P and Ti anomalies for the alkali riebeckite granite (Fig. 8a) suggest the important role of K-feldspar and/or biotite, Fe–Ti oxide and apatite fractionation. In the fractionation diagrams (Fig. 13c, d, e), the chemical variation in the alkali riebeckite granite can be attributed to the fractional crystallization of mainly plagioclase and K-feldspar along with hornblende and biotite.

The fractional crystallization hypothesis for the chemical variation can be tested using the conventional least-squares mixing calculations devised by Wright and Doherty (1970). The results of the calculations are given in Table 7. For calculations, the sample with the lower silica value (sample# 160) was used as the parent composition, and the sample with the higher silica value (sample# 153) as the daughter. The calculations show that sample# 153 could be produced from sample# 160 by 24 % crystallization of plagioclase (13.6 %), K-feldspar (7.2 %), amphibole (2.5 %) and biotite (0.06 %), with residual liquid (daughter) (75.5 %). So, the investigated alkali riebeckite granites in the Abu Kharif area were generated by 65 % batch melting of metasomatized Pan-African granite source followed by fractional crystallization of plagioclase, K-feldspar, amphibole and biotite with minor magnetite, apatite and titanite.

**Table 5.** Results of fractionation modelling for the monzogranite based on the method of Wright and Doherty (1970)

Fractionation of the monzogranite (from sample# 110 to sample# 115)								
Fractionation phases								
	Plagioclase	K-feldspar	Biotite	Magnetite	Ilmenite	Observed daughter	Observed parent	Calculated parent
<b>SiO<sub>2</sub></b>	69.1	65.1	38.1	0.00	0.00	77.59	74.96	76.02
<b>TiO<sub>2</sub></b>	0.00	0.01	2.64	0.72	0.02	0.13	0.24	0.23
<b>Al<sub>2</sub>O<sub>3</sub></b>	18.41	19.2	13.37	0.2	49.58	12.25	12.84	12.98
<b>FeO*</b>	0.02	0.00	16.98	91.31	49.84	0.72	1.38	1.39
<b>MnO</b>	0.01	0.03	0.48	0.00	0.00	0.01	0.01	0.02
<b>MgO</b>	0.00	0.00	14.73	0.00	0.11	0.06	0.38	0.4
<b>CaO</b>	0.41	0.01	0.01	0.00	0.00	0.68	1.23	0.9
<b>Na<sub>2</sub>O</b>	10.61	0.41	0.13	0.00	0.00	3.99	3.95	4.04
<b>K<sub>2</sub>O</b>	0.13	14.91	9.57	0.00	0.00	3.99	3.95	4.02

Parent (sample# 110) = 88.59 % daughter (sample# 115) + 6.12 % plag. + 2.33 % biotite + 2.39 % K-feld. + 0.88 % Mag. + 0.11 % Ilm fractionated phases (11.83 %): 51.73 % plag., 19.7 % biotite, 20.2 % K-feld., 7.44 % Mag., 0.93 % Ilm.

$R^2=1.17$ .

The composition of plagioclase, K-feldspar and biotite are after Moghazi *et al.* (2011), while the composition of magnetite and ilmenite are after Deer *et al.* (1978).  $R^2$ : sum of squares of the residual.

### 5.c. The Abu Kharif intrusions as sources for tungsten mineralization

All major tungsten deposit types – among the rare metals – are associated with granitic intrusions or with medium- to high-grade metamorphic rocks (Brown & Pitfield, 2014). Generally, rare metals-bearing granites occur in subduction-related environments, but dominantly in a late-orogenic to post-orogenic setting (e.g. Richards, 2011). The mineralized plutons are commonly identified as extremely fractionated alkaline granites, and their sources seem to be dominated by: (i) primary magmatic origin, where the prolonged crystallization of quartz and feldspar yields a late-stage magmatic fluid enriched in volatiles (H<sub>2</sub>O, F) and trace elements (e.g. Dostal & Chatterjee, 1995; Agangi *et al.* 2010), and (ii) secondary metasomatic origin, where a hydrothermal fluid, unrelated to the magma, could have leached the trace elements from the host rocks (Nurmi & Haapala, 1986). In both models, complexation of rare metals with volatiles such as F, Cl and CO<sub>2</sub> can significantly increase the solubility of trace elements (Salvi & Williams-Jones, 2005; Schönerberger *et al.* 2008; Agangi *et al.* 2010). Of particular interest, the F-bearing fluids have the ability to transport lithophile immobile elements as indicated by the presence of REE- and HFSE-bearing minerals (e.g. zircon and fluorite), especially in the alkali-feldspar granite. Another controversial issue is the source of tungsten. Generally, two sources have been suggested for tungsten mineralization in granitic magmas. These sources include mantle source from mafic magmas (e.g., Carten *et al.* 1993; Audétat, 2010) and a predominant crustal source (e.g. Sinclair, 2007; Mao *et al.* 2011), where certain crustal rocks contain much more tungsten than mafic magmas. In the Earth's continental crust, the average tungsten abundance is estimated to be 1.5 ppm (Rudnick & Gao, 2003).

The enrichment mechanism of tungsten in the Abu Kharif area is controlled by many factors such as degree of rock fractionation, availability of volatiles (i.e. F and H<sub>2</sub>O), and structural elements (El-Desouky, 2005; Abdel-Rahman, 2006). Tungsten is detected in all the studied granite plutons but with different degrees of enrichment (Table 2). The magma sources for the studied granite types are here considered to be the continental crust (Section 5.b.

above). Therefore, the continental crust would be the W source. Many authors use the Zr/Hf ratio to investigate the degree of rare metals enrichment in the original magma, since Zr/Hf ratio is constant in most geological systems (Dostal & Chatterjee, 1995; Linnen & Keppler, 2002). However, the decrease of the Zr/Hf ratio in granitic melt is associated with enrichment in rare metals such as W, Mo, Sn, Bi, Be, Ta, Nb and Li, up to concentrations sufficient to form deposits (Zaraisky *et al.* 2009). The whole-rock geochemical data of the studied granitic plutons show that the Zr/Hf ratios of the monzogranite (29.74 ppm, on average) are far lower than those for the granodiorite (39.14 ppm, on average) and the alkali riebeckite granite (42.58 ppm, on average). This may indicate that the monzogranite is originally more enriched in W compared to the granodiorite and alkali riebeckite granites. On the other hand, the alkali riebeckite granite is rich in silica and alkalis (Table 1) with geochemical signatures typical of an iron-rich and oxidized nature rather than the granodiorite and monzogranite. This iron-rich oxidized granite is considered a suitable rock for hosting tungsten, where W is an incompatible element and likely to remain in the residual melts and consequently is closely confined to the fractionated granite. Nevertheless, the alkali riebeckite granite in the Abu Kharif area shows low content of W (2.53 ppm, on average) compared to the granodiorite (8.11 ppm, on average) and monzogranite (4.3 ppm, on average) (Table 2). This may be a result of potential factors limiting W enrichment in the residual melts, such as W removal by exsolving fluids.

The field and petrographic investigations show that all granite intrusions in the study area have been affected by the magmatic-related hydrothermal fluids, but the monzogranite seems to be strongly affected by alteration in comparison with the granodiorite and alkali riebeckite granites. Textural and compositional evidences for hydrothermal alteration in the monzogranite are: (1) Nametasomatism in the form of perthite crystals, where twinned and untwinned albite occurs as fine laths and rims around K-feldspar, suggesting albitization through interaction with hydrothermal fluids, (2) abundance of alteration minerals due to greisenization such as chlorite after biotite, sericite after feldspars, and silicification, (3) widespread occurrence of F-bearing minerals such as fluorite in the form of interstitial accessory mineral and

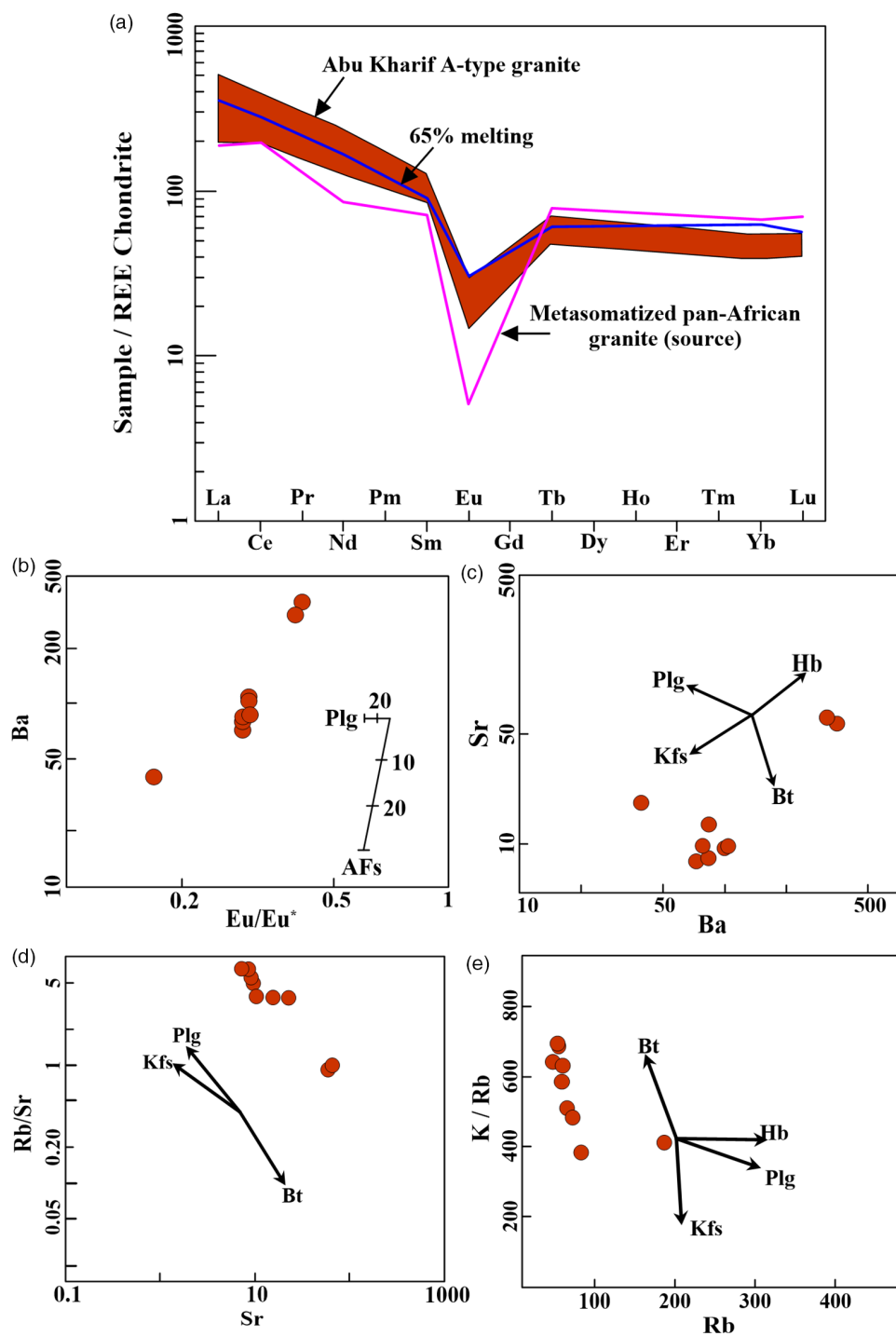


**Fig. 13.** (Colour online) (a) Chondrite-normalized diagram showing the matching of the REE field pattern of the studied A1-type alkali riebeckite granite with 65 % non-modal batch melting of metasomatized Pan-African granites. The composition of the metasomatized granite source is after Abdel-Rahman (2006). Normalization values are taken from Taylor and McLennan (1985). (b) Ba vs  $Eu/Eu^*$  (Eby, 1990); (c) Ba vs Sr (fractionation factors from Inger & Harris, 1993); (d) Sr vs Rb/Sr (fractionation factors from Inger & Harris, 1993); (e) Rb vs K/Rb. Plg = plagioclase, Hb = hornblende, Kfs = K-feldspar and Bt = biotite. Symbols as Fig. 10.

veins cutting through granite indicating that F-rich fluids have affected the granites, and (4) intense silicification of the wall rocks and formation of the quartz veins. Geometric and textural features of quartz veins indicate multistage opening and mineralization being probably associated with the youngest stage in the paragenetic sequence.

The field study indicates that the wolframite-bearing quartz veins and associated alteration are displayed on a set of N40°E–S40°W-trending fracture-filling veins with low dip ranging from 8° up to 25° toward the NW. Therefore, the Abu Kharif wolframite mineralization is classified as the vein-type ores that are associated

with late-stage hydrothermal activity. Progressive cooling of the fluids led to the precipitation of W; the amount of soluble tungsten in hydrothermal ore fluids falls rapidly with decreasing temperature and this is more pronounced at a temperature around 300 °C (Heinrich, 1990). The late stage of the magmatic intrusions of the studied alkali riebeckite granite is associated with an abundance of hydrothermal fluids. These fluids are forced to move due to the pressure release caused by faulting along the NE–SW coevally formed shear zones.

Based on the above discussion, a model for generation of granite rock types as well as tungsten mineralization in the Abu Kharif area

**Table 6.** Results of rare earth elements non-modal batch melting modelling for different degrees of metasomatized Pan-African granite source

	Source	D <sub>0</sub>	P	Calculated melt			Observed melt
				F = 55 %	F = 60 %	F = 65 %	
<b>La</b>	43.80	0.385	0.765	85.17	83.27	81.45	80.90
<b>Ce</b>	116.80	0.530	0.740	173.55	170.26	167.10	168.10
<b>Nd</b>	38.30	2.771	4.470	44.41	55.59	74.30	71.20
<b>Sm</b>	10.50	1.820	2.570	10.98	11.96	13.13	12.76
<b>Eu</b>	0.29	5.000	8.430	0.32	0.54	1.70	1.63
<b>Tb</b>	2.85	2.244	2.435	1.96	2.06	2.17	1.71
<b>Yb</b>	10.90	1.620	1.829	9.36	9.71	10.08	6.26
<b>Lu</b>	1.67	1.764	1.820	1.27	1.31	1.36	0.98

The metasomatized pan-African calc-alkaline source composition is after Abdel-Rahman and Martin (1990). Observed melt = compositions of the least evolved sample of the alkali riebeckite granite (sample# 160). The used distribution coefficients are after Rollinson (1993) and GERM (Geochemical Earth Reference Model; <http://www.earthref.org/GERM>). D<sub>0</sub> = bulk distribution coefficient for the starting assemblage, P = bulk distribution coefficient of the minerals that make up the melt, F = melt fraction.

**Table 7.** Results of fractionation modelling for the alkali riebeckite granite based on the method of Wright and Doherty (1970)

Fractionation of the alkali riebeckite granite (from sample# 160 to sample# 153)							
Fractionation phases							
	Plagioclase	K-feldspar	Amphibole	Biotite	Observed daughter	Observed parent	Calculated parent
<b>SiO<sub>2</sub></b>	67.56	65.01	46.49	36.30	69.63	75.45	76.35
<b>TiO<sub>2</sub></b>	0.00	0.00	1.76	1.76	0.47	0.25	0.13
<b>Al<sub>2</sub>O<sub>3</sub></b>	20.09	18.09	1.53	16.11	13.98	12.04	12.09
<b>FeO*</b>	0.00	0.18	32.3	23.05	3.28	2.27	2.26
<b>MnO</b>	0.00	0.00	0.85	0.81	0.01	0.01	0.04
<b>MgO</b>	0.00	0.00	0.26	6.39	1.59	0.01	0.22
<b>CaO</b>	0.73	0.00	6.12	0.03	3.58	0.59	0.12
<b>Na<sub>2</sub>O</b>	11.47	0.32	7.87	0.00	4.20	4.25	4.41
<b>K<sub>2</sub>O</b>	0.13	16.25	0.91	8.56	1.94	4.10	4,197

Parent (sample# 160) = 75.49 % daughter (sample# 153) + 13.55 % plagioclase + 7.19 % K-feld. + 2.49 % Hb + 0.06 % biotite.

Fractionating phases (23.29 %): 58.18 % plagioclase, 30.87 % K-feldspar, 10.69 % amphibole and 0.24 % biotite.

R<sup>2</sup> = 0.94.

Plagioclase and biotite compositions are after MM El-Sayed (unpub. PhD thesis, Alexandria Univ., 1994) while the composition of K-feldspar and amphibole are after Abdel-Rahman (2006). R<sup>2</sup>: sum of squares of the residual.

can be proposed (Fig. 14). The studied granite types represent different magmatic pulses, where the granodiorite was derived from the melting of amphibolitic lower continental crust, whereas the monzogranite and alkali riebeckite granite were derived from the melting of Pan-African middle to upper continental crust (Fig. 14). These parent magmas were originally rich in W, but with different concentrations. The highly fractionated and oxidized nature and volatile content of monzogranite and alkali riebeckite granite provided a critical factor that affects W behaviour and led to the original enrichment in W. Prolonged fractional crystallization in the monzogranite and alkali riebeckite granite led the rest melt to become volatile enrichment (H<sub>2</sub>O, F). Progressive cooling of this magma was finalized by silica-rich fluids characterized by high viscosity, low density and enrichment in W and volatiles. These hydrothermal fluids could easily leach W from the wall rocks along the conduit (Fig. 14). The mineralized fluids were circulated through the fracture elements that dominated in the monzogranite rather than the other granitic plutons. Additionally, albitization, greisenization and silicification due to reactions of the circulating fluids with the wall rocks occur widely. Obviously, the intensity of

alteration in monzogranite is more distinct than in the granodiorite and alkali riebeckite granite.

## 6. Conclusions

The Abu Kharif area in the Northern Eastern Desert of Egypt comprises granodiorite, monzogranite and alkali riebeckite granite. The granodiorite is classified as late-orogenic I-type calc-alkaline granite, whereas the monzogranite is post-orogenic and has highly fractionated affinity. On the other hand, the alkali riebeckite granite displays anorogenic A1-subtype alkaline affinity. Field observations and chemical features indicate that the three granite rock types are not genetically related, but they represent separate magmatic pulses originated from different sources. The granodiorite was generated by ~75 % melting of lower crustal amphibolitic source followed by fractional crystallization of hornblende, biotite, apatite and titanite. However, both the monzogranite and alkali riebeckite granite were produced by crustal anatexis of Pan-African granitic source. The monzogranite was formed by 62 % batch partial melting of non-metasomatized crust followed by a

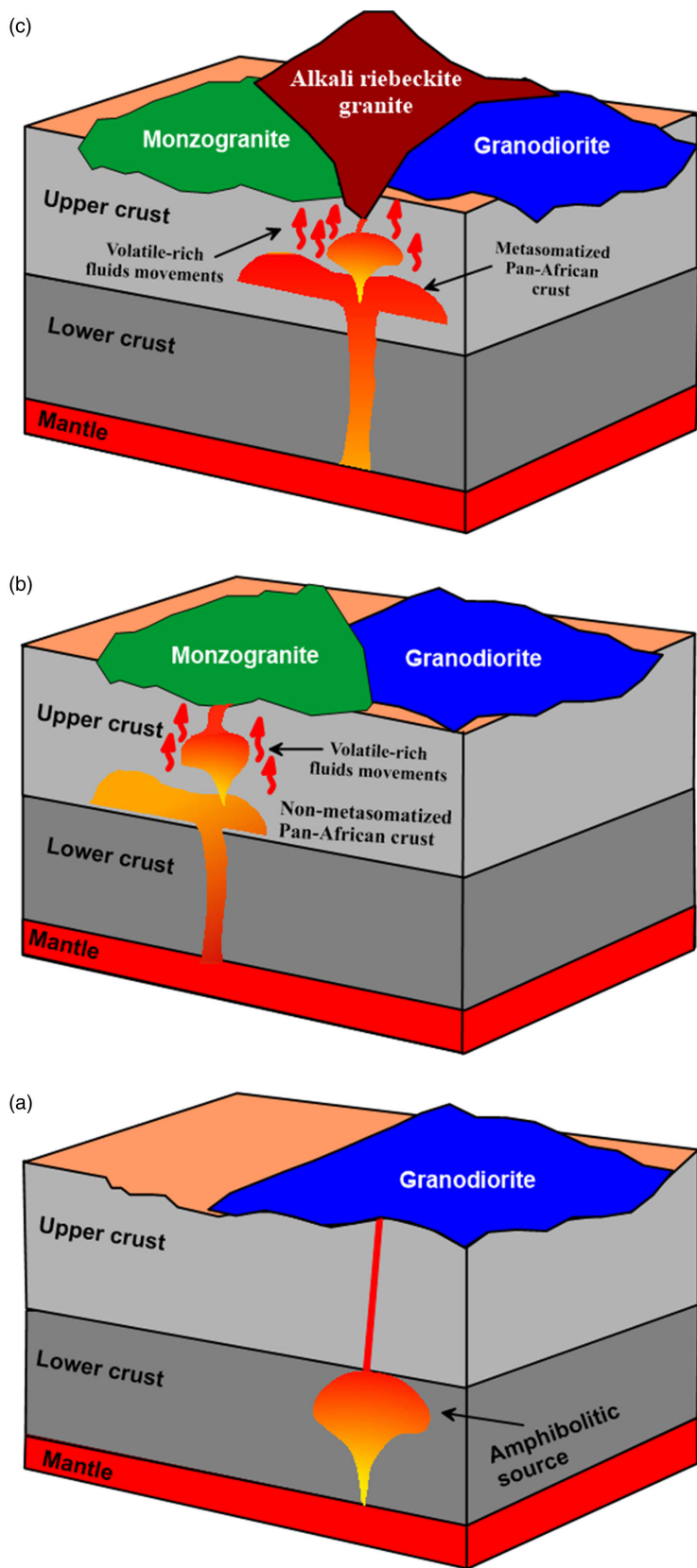


**Fig. 14.** (Colour online) Sketch model illustrating the genesis of contrasting granite rock types in the Abu Kharif area. (a) The Cryogenian granodiorite (~650 Ma) was generated by batch partial melting of an amphibolitic source followed by fractional crystallization. (b) The Ediacaran wolframite-bearing monzogranite (610–580 Ma) was formed by batch partial melting of the normal ‘non-metasomatized’ Pan-African crust of calc-alkaline granite composition followed by fractional crystallization. (c) The Cambrian alkali riebeckite granite (522 Ma) was generated by batch partial melting of metasomatized Pan-African granite source followed by fractional crystallization.

role of crystallization of plagioclase, biotite, K-feldspar, magnetite, ilmenite, apatite and titanite. On the other hand, the alkali riebeckite granite was produced by 65 % batch partial melting of

metasomatized crust followed by fractional crystallization of plagioclase, K-feldspar, amphibole and biotite with minor magnetite, apatite and titanite.

The variation in W content in the original magmas seems to be controlled by the degree of rock fractionation and availability of volatiles such as F and H<sub>2</sub>O. The W enrichment in the monzogranite is interpreted to be formed by magmatic-related hydrothermal volatile-rich fluids. These hydrothermal fluids are suggested to be related to the youngest magma in the study area that produced the alkali riebeckite granite. Tungsten was transported through silica-rich aqueous fluids to the cupola of the magma chamber by the power of volatiles that ejected from the parental magma. The fluids are forced to move due to the pressure release caused by faulting along the NE–SW coevally formed shear zones.

**Acknowledgements.** The authors would like to express their deepest gratitude and appreciation to Dr Hassan El-Sundoly, Nuclear Materials Authority, for his great help and guidance during the field work. The journal editor and anonymous reviewers are gratefully acknowledged for their valuable suggestions which led to the improvement of the manuscript. This research received no specific grant from any funding agency, commercial or not-for-profit sectors.

**Conflict of interest.** Nora G Abdel Wanees, Mohamed M El-Sayed, Khalil I Khalil and Hossam A Khamis declare that they have no conflict of interest.

**Human/animal rights.** This article does not contain any studies with human or animal subjects performed by any of the authors.

## References

- Abd El-Ghaffar NI and Ramadan AA (2018) Geochemistry and origin of alkaline granites at Wadi Umm Adawi-Yahmid area, South Sinai, Egypt. *Journal of African Earth Science* **146**, 66–77.
- Abd El-Wahed MA and Abu Anbar MM (2009) Syn-oblique convergent and extensional deformation and metamorphism in the Neoproterozoic rocks along Wadi Fatira shear zone, Northern Eastern Desert, Egypt. *Arabian Journal of Geoscience* **2**, 29–52.
- Abdel-Rahman AM (2006) Petrogenesis of anorogenic peralkaline granitic complexes from Eastern Egypt. *Mineralogy Magazine* **70**, 27–50.
- Abdel-Rahman AM (2021) Petrogenesis of a rare Ediacaran tonalite–trondhjemite–granodiorite suite, Egypt, and implications for Neoproterozoic Gondwana assembly. *Geological Magazine* **158**, 701–22. doi: [10.1017/S0016756820000795](https://doi.org/10.1017/S0016756820000795).
- Abdel-Rahman AM and El-Kibbi MM (2001) Anorogenic magmatism: chemical evolution of the Mount El-Sibai A-type complex (Egypt), and implications for the origin of within-plate felsic magmas. *Geological Magazine* **138**, 67–85.
- Abdel-Rahman AM and Martin RF (1990) The Mount Gharib A-type granite, Nubian shield: petro-genesis and role of metasomatism at the source. *Contributions to Mineralogy and Petrology* **104**, 173–83.
- Abu Sharib AS, Maurice AE, Abd El-Rahman YM, Sanislav IV, Schulz B, Bottros R and Bakhit BR (2019) Neoproterozoic arc sedimentation, metamorphism and collision: evidence from the northern tip of the Arabian-Nubian Shield and implication for the terminal collision between East and West Gondwana. *Gondwana Research* **66**, 13–42.
- Agangi A, Kamenetsky VS and McPhie J (2010) The role of fluorine in the concentration and transport of lithophile trace-elements in felsic magmas: insights from the Gawler Range Volcanics, South Australia. *Chemical Geology* **273**, 314–25.
- Agrawal S (1995) Discrimination between late-orogenic, post-orogenic, and anorogenic granites by major elements composition. *The Journal of Geology* **103**, 525–37.
- Akaad MK and Abu El-Ela AM (2002) *Geology of the basement rocks in the eastern half of the belt between latitudes 2530 and 2630N Central Eastern Desert, Egypt*. Geological Survey of Egypt, Paper no. 78.
- Ali KA, Moghazi AM, Maurice AE, Omar SA, Wang Q, Wilde SA, Moussa EM, Manton WI and Stern RJ (2012) Composition, age, and origin of the ~620 Ma Humr Akarim and Humrat Mukbid A-type granites: no evidence for pre Neoproterozoic basement in the Eastern Desert, Egypt. *International Journal of Earth Science* **101**, 1705–22.
- Ali SA, Ismail SA, Nutman AP, Bennett VC, Jones BG and Buckman S (2016) The intra-oceanic Cretaceous (~108 Ma) Rata–Rash arc fragment in the North segment of Iraqi Zagros suture zone: implications for Neo-Tethys evolution and closure. *Lithos* **260**, 154–63.
- Altherr R, Holl A, Hegner E, Langer C and Kreuzer H (2000) High-potassium, calc-alkaline I-type plutonism in the European Variscides: northern Vosges France and northern Schwarzwald, Germany. *Lithos* **50**, 51–73.
- Anderson JL and Cullers RL (1978) Geochemistry and evolution of the Wolf River batholith, a late Precambrian rapakivi massif in north Wisconsin, U.S.A. *Precambrian Research* **7**, 287–324.
- Audétat A (2010) Source and evolution of molybdenum in the porphyry Mo (–Nb) deposit at cave peak, Texas. *Journal of Petrology* **51**, 1739–60.
- Bailey DK (1974) Origin of alkaline magmas as a result of anatexis, (b) crustal anatexis. In *The Alkaline Rocks* (ed H Sorenson), pp. 436–42. London: Wiley.
- Barboni M and Bussy F (2013) Petrogenesis of magmatic albite granites associated to cogenetic A-type granites: Na-rich residual melt extraction from a partially crystallized A-type granite mush. *Lithos* **177**, 328–51.
- Basta FF, Maurice AE, Bakhit BR, Azer MK and El-Sobkyf AF (2017) Intrusive rocks of the Wadi Hamad Area, North Eastern Desert, Egypt: change of magma composition with maturity of Neoproterozoic continental island arc and the role of collisional plutonism in the differentiation of arc crust. *Lithos* **288–289**, 248–63.
- Brown T and Pitfield P (2014) Tungsten. In *Critical Metals Handbook* (ed G Gunn), pp. 365–410. Keyworth, Nottingham: British Geological Survey.
- Carten RB, White WH and Stein HJ (1993) High-grade granite-related molybdenum systems: classification and origin. *Geological Association of Canada, Special Paper no. 40*, 521–54.
- Chappell BW and White AJR (1974) Two contrasting granite types. *Pacific Geology* **8**, 173–4.
- Clemens JD and Stevens G (2012) What controls chemical variations in granitic magma? *Lithos* **134–135**, 317–29.
- Cox GM, Lewis CJ, Collins AS, Halverson GP, Jourdan F, Foden J, Nettle D and Kattan F (2012) Ediacaran terrane accretion within the Arabian-Nubian Shield. *Gondwana Research* **21**, 341–52.
- De la Roche H, Leterrier J, Granclaude P and Marchal M (1980) A classification of volcanic and plutonic rocks using R1-R2 diagram and major-element analyses: its relationships with current nomenclature. *Chemical Geology* **29**, 183–210.
- Debon F and Le Fort P (1983) A chemical-mineralogical classification of common plutonic rocks and associations. *Transactions of the Royal Society of Edinburgh Earth Sciences* **73**, 135–49.
- Deer WA, Howie RA and Zussman J (1978) *Rock-Forming Minerals, v. 2A, Single Chain Silicates*, 2nd edn. London: Longmans.
- Dewitt E (1989) Geochemistry and tectonic polarity of early Proterozoic (1700–1750 Ma) plutonic rocks, northcentral Arizona. In *Geologic Evolution of Arizona* (eds JP Jenney and SI Raynold), pp. 149–64. Arizona: Arizona Geological Society Digest 17.
- Dostal J and Chatterjee AK (1995) Origin of topaz-bearing and related peraluminous granites of the late Devonian Davis Lake pluton, Nova Scotia, Canada: crystal versus fluid fractionation. *Chemical Geology* **123**, 67–88.
- Douce PAE (1996) Effects of pressure and H<sub>2</sub>O content on the compositions of primary crustal melts. *Transactions of the Royal Society of Edinburgh Earth Science* **87**, 11–21.
- Douce PAE and Beard JS (1995) Dehydration-melting of biotite gneiss and quartz amphibolite from 3 to 15 kbar. *Journal of Petrology* **36**, 707–38.
- Douce PAE and Beard JS (1996) Effects of P, fO<sub>2</sub> and Mg/Fe ratio on dehydration melting of model metagreywackes. *Journal of Petrology* **37**, 999–1024.
- Douce AEP and McCarthy TC (1998) Melting of crustal rocks during continental collision and subduction. In *When Continents Collide: Geodynamics and Geochemistry of Ultrahigh-Pressure Rocks* (eds BR Hacker and JG Liou), pp. 27–55. Dordrecht: Springer.
- Eby GN (1990) The A-type granitoids: a review of their occurrence and chemical characteristics and speculations on their petrogenesis. *Lithos* **26**, 115–34.



- Eby GN** (1992) Chemical subdivision of the A-type granitoids: petrogenetic and tectonic implications. *Geology* **20**, 641–4.
- El Bahariya GA** (2018) Classification of the Neoproterozoic ophiolites of the Central Eastern Desert, Egypt based on field geological characteristics and mode of occurrence. *Arabian Journal of Geosciences* **11**, 313.
- El-Bialy MZ** (2020) Precambrian basement complex of Egypt. In *The Geology of Egypt* (eds Z Hamimi, A El-Barkooky, J Martínez Frias, F Harald & Y Abd El-Rahman), pp. 37–79. Cham: Springer Nature Switzerland.
- El-Bialy MZ and Hassen IS** (2012) The late Ediacaran (580–590 Ma) onset of anorogenic alkaline magmatism in the Arabian–Nubian Shield: Katherina A-type rhyolites of Gabal Ma'ain, Sinai, Egypt. *Precambrian Research* **216**, 1–22.
- El-Bialy MZ and Omar MM** (2015) Spatial association of Neoproterozoic continental arc I-type and post-collision A-type granitoids in the Arabian–Nubian Shield: the Wadi Al-Baroud older and younger granites. *African Earth Sciences* **103**, 1–29.
- El-Desouky H** (2005) *Economic mineralizations in the area of Abu Kharif Mountain, Northern Eastern Desert, Egypt: a combined remote sensing and geochemistry study after field work*. MSc thesis, Vrije Universiteit, Brussel, Brussels, Belgium, 164 pp. Published thesis.
- Eliwa HH, Ramadan EM and Nosair AM** (2014) Water/land use planning of Wadi El-Arish watershed, Central Sinai, Egypt using RS, GIS and WMS techniques. *International Journal of Science and Engineering Research* **5**, 341–9.
- El-Mahallawi MM and Ahmed AF** (2012) Late Proterozoic older granitoids from the North Eastern desert of Egypt: petrogenesis and geodynamic implications. *Arabian Journal of Geoscience* **5**, 15–27.
- El-Sayed MM** (1998) Tectonic setting and petrogenesis of the Kadabora pluton: a late Proterozoic anorogenic A-type younger granitoid in the Egyptian Shield. *Chemie der Erde – Geochemistry* **58**, 38–63.
- El-Sayed MM** (2003) The Neoproterozoic Dubr intrusives, Central Eastern Desert, Egypt: petrological and geochemical constraints on the evolution of a mafic-felsic suite. *Neues Jahrbuch Mineralogie – Abhandlungen* **179**, 1–42.
- El-Sayed MM, Furnes H and Mohamed FH** (1999) Geochemical constraints on the tectonomagmatic evolution of the late Precambrian Fawakhir ophiolite, central Eastern Desert, Egypt. *Journal of African Earth Science* **29**, 515–33.
- El-Sayed MM, Furnes H, Obeid MA and Hassanen MA** (2001) The Mueilha intrusion, Eastern Desert, Egypt: a post-orogenic, peraluminous, rare metal bearing granite. *Chemie der Erde – Geochemistry* **61**, 294–316.
- El-Shazly SM and El-Sayed MM** (2000) Petrogenesis of the Pan-African El Bula igneous suite, central Eastern Desert, Egypt. *Journal of African Earth Science* **31**, 317–36.
- Farahat ES and Azer MK** (2011) Post-collisional magmatism in the northern Arabian–Nubian Shield: the geotectonic evolution of the alkaline suite at Gebel Tarbush area, south Sinai, Egypt. *Chemie der Erde – Geochemistry* **71**, 247–66.
- Farahat ES, Mohamed HA, Ahmed AF and El-Mahallawi MM** (2007) Origin of I and A-type granitoids from the Eastern Desert of Egypt: implications for crustal growth in the northern Arabian–Nubian Shield. *Journal of African Earth Sciences* **49**, 43–58.
- Farahat ES, Zaki R, Hauzenberger C and Sami M** (2011) Neoproterozoic calc-alkaline peraluminous granitoids of the Delehimmi pluton, Central Eastern Desert, Egypt: implications for transition from late- to post-collisional tectonomagmatic evolution in the northern Arabian–Nubian Shield. *Geology* **46**, 544–60.
- Foley SF, Barth MG and Jenner GA** (2000) Rutile/melt partition coefficients for trace-elements and an assessment of the influence of rutile on the trace-element characteristics of subduction zone magmas. *Geochimica et Cosmochimica Acta* **64**, 933–8.
- Frost BR, Barnes CG, Collins WJ, Arculus RJ, Ellis DJ and Frost CD** (2001) A geochemical classification for granitic rocks. *Journal of Petrology* **42**, 2033–48.
- Frost BR and Frost CD** (2008) A geochemical classification for feldspathic igneous rocks. *Journal of Petrology* **49**, 1955–69.
- Frost CD and Frost BR** (2010) On Ferroan (A-type) Granitoids: their compositional variability and modes of origin. *Journal of Petrology* **52**, 39–53.
- Frost CD, Frost BR, Bell JM and Chamberlain KR** (2002) The relationship between A-type granites and residual magmas from anorthosite: evidence from the northern Sherman batholith, Laramie Mountains, Wyoming, USA. *Precambrian Research* **119**, 45–71.
- Furnes H, El-Sayed MM, Khalil SO and Hassanen MA** (1996) Pan African magmatism in the Wadi El-Imra district, Central Eastern Desert, Egypt: geochemistry and tectonic environment. *Journal of the Geological Society of London* **153**, 705–18.
- Gao P, Zhao ZF and Zheng YF** (2016) Magma mixing in granite petrogenesis: insights from biotite inclusions in quartz and feldspar of Mesozoic granites from South China. *Journal of Asian Earth Science* **123**, 142–61.
- Garcia D, Fonteilles M and Moutte J** (1994) Sedimentary fractionation between Al, Ti, and Zr and the genesis of strongly peraluminous granites. *Geology* **102**, 411–22.
- Gardien V, Thompson AB, Grujic D and Ulmer P** (1995) Experimental melting of biotite + plagioclase + quartz ± muscovite assemblage and implications for crustal melting. *Journal of Geophysical Research* **100**, 15581–91.
- Green TH** (1980) Island arc and continent-building magmatism: a review of petrogenetic models based on experimental petrology and geochemistry. *Tectonophysics* **63**, 367–85.
- Harris NB, Pearce JA and Tindle AG** (1986) Geochemical characteristics of collision-zone magmatism. In *Collision Tectonics* (eds MP Coward and AC Ries), pp. 67–81. Geological Society of London, Special Publication no. 19.
- Heinrich CA** (1990) The chemistry of hydrothermal tin (–tungsten) ore deposition. *Economic Geology* **85**, 457–81.
- Helba H, Trumbull RB, Morteani G, Khalil SO and Arslan A** (1997) Geochemical and petrographic studies of Ta mineralization in the Nuweibi albite granite complex, Eastern Desert, Egypt. *Mineralium Deposita* **32**, 164–79.
- Inger S and Harris N** (1993) Geochemical constraints on leucogranite magmatism in the Langtang Valley, Nepal Himalaya. *Journal of Petrology* **34**, 345–68.
- Jacobs J and Thomas RJ** (2004) Himalayan-type indenter-escape tectonics model for the southern part of the late Neoproterozoic-early Paleozoic East African Antarctic orogen. *Geology* **32**, 721–4.
- Jarrar G, Stern RJ, Saffarinai G and Al-Zubi H** (2003) Late- and post-orogenic Neoproterozoic intrusions of Jordan: implications for crustal growth in the northernmost segment of the East African Orogen. *Precambrian Research* **123**, 295–319.
- Johnson PR, Halverson GP, Kusky TM, Stern RJ and Pease V** (2013) Volcanosedimentary basins in the Arabian–Nubian shield: markers of repeated exhumation and denudation in a Neoproterozoic accretionary orogen. *Geosciences* **3**, 389–445.
- Juan W and Xin L** (2009) Petrogenesis and geochemistry of the host monzogranite and mafic enclaves from the Triassic Wulong pluton in South Qinling, central China. *Chinese Journal of Geochemistry* **28**, 432–9.
- Jung S, Mezger K and Hoernes S** (1998) Petrology and geochemistry of syn- to post-collisional metaluminous A type granites: a major and trace-element and Nd-Sr-P-isotope study from the Proterozoic Damara Belt, Namibia. *Lithos* **45**, 147–75.
- Kusky TM, Abdelsalam M, Stern RJ and Tucker RD** (2003) Evolution of the East African and related orogens, and the assembly of Gondwana. *Precambrian Research* **123**, 81–5.
- Küster D and Harms U** (1998) Post-collisional potassic granitoids from the southern and northwestern parts of the Late Neoproterozoic East African Orogen: a review. *Lithos* **45**, 177–95.
- Liégeois JP and Black R** (1987) Alkaline magmatism subsequent to collision in the Pan-African belt of the Adrar des Iforas (Mali). In *Alkaline Igneous Rocks* (eds JG Fitton and BGJ Upton), pp. 381–401. Geological Society of London, Special Publication no. 30.
- Lindh A, Abu El-Rus MA, Mohamed MA, Persson P and Scherstén A** (2019) A model for granite evolution based on non-equilibrium magma separation:

- evidence from the Gharib and Qattar fluorite-bearing granites, Eastern Desert, Egypt. *International Journal of Earth Sciences* **108**, 1201–32.
- Linnen RL and Keppler H** (2002) Melt composition control of Zr/Hf fractionation in magmatic processes. *Geochimica et Cosmochimica Acta* **66**, 3293–301.
- Mahdy NM, El Kalioubi BA, Wohlgenuth-Ueberwasser CC, Shalaby MH and El-Afandy AH** (2015) Petrogenesis of U- and Mo-bearing A2-type granite of the Gattar batholith in the Arabian Nubian Shield, Northeastern Desert, Egypt: evidence for the favorability of host rocks for the origin of associated ore deposits. *Ore Geology Reviews* **71**, 57–81.
- Mao J, Pirajno F and Cook N** (2011) Mesozoic metallogeny in East China and corresponding geodynamic settings: an introduction to the special issue. *Ore Geology Reviews* **43**, 1–7.
- Mao QG, Xiao WJ, Fang TH, Windley BF, Sun M, Ao SJ, Zhang JE and Huang XK** (2014) Geochronology, geochemistry and petrogenesis of Early Permian alkaline magmatism in the Eastern Tianshan: implications for tectonics of the Southern Altai. *Lithos* **190–191**, 37–51.
- McDonald RM, Davies GR, Bliss CM, Leat PT, Bailey DK and Smith RL** (1987) Geochemistry of high-silica peralkaline rhyolites, Naivasha, Kenya Rift Valley. *Journal of Petrology* **28**, 979–1008.
- McDonough W and Sun SS** (1995) The composition of the Earth. *Chemical Geology* **67**, 1050–6.
- Moghazi AM** (1999) Magma source and evolution of Late Neoproterozoic granitoids in the Gabal El-Urf area, Eastern Desert, Egypt: geochemical and Sr–Nd isotopic constraints. *Geological Magazine* **136**, 285–300.
- Moghazi AM** (2002) Petrology and geochemistry of Pan-African granitoids, Kab Amiri area, Egypt: implications for tectonomagmatic stages in the Nubian Shield evolution. *Mineralogy and Petrology* **75**, 41–67.
- Moghazi AM, El-Sayed MM, Arslan AI and Hosny H** (2004) Geochemistry and petrogenesis of the Late Neoproterozoic granitoids at Wadi Hammed, Northern Eastern Desert, Egypt. 6th Inter Conference on Geochemistry, Alexandria University, Egypt, Abstract 200, p. 144.
- Moghazi AM, Iaccheri LM, Bakhsh RA, Koto AB and Ali KA** (2015) Sources of rare-metal-bearing A-type granites from Jabal El-Sayed complex, Northern Arabian Shield, Saudi Arabia. *Journal of Asian Earth Sciences* **107**, 244–58.
- Moghazi N., Emam AA and Abdel-Rahman EM** (2011) Mineral chemistry and geochemical aspects of Gebel Filat granites, South Eastern Desert, Egypt. *Arabian Journal of Geoscience* **4**, 689–702.
- Mohamed HA, Ali S, Sedki T and Abdel Khalik II** (2019) The Sukari Neoproterozoic granitoids, Eastern Desert, Egypt: petrological and structural implications. *Journal of African Earth Sciences* **149**, 426–40.
- Mushkin A, Navon O, Halicz L, Hartmann G and Stein M** (2003) The petrogenesis of A-type magmas from the Amram massif, southern Israel. *Journal of Petrology* **44**, 815–32.
- Nurmi PA and Haapala I** (1986) The Proterozoic granitoids of Finland: granite types, metallogeny and relation to crustal evolution. *Bulletin of the Geological Society of Finland* **58**, 431–53.
- Pearce JA** (1996) Sources and settings of granitic rocks. *Episodes* **19**, 120–5.
- Pearce JA, Harris NBW and Tindle AG** (1984) Trace-element discrimination diagrams for the tectonic interpretation of granitic rocks. *Journal of Petrology* **25**, 956–83.
- Richards JP** (2011) High Sr/Y arc magmas and porphyry Cu ± Mo ± Au deposits: just add water. *Economic Geology* **106**, 1075–81.
- Rollinson HR** (1993) *Using Geochemical Data: Evaluation, Presentation, Interpretation*. Harlow and New York: Longman/Wiley.
- Rudnick R and Gao S** (2003) Composition of the continental crust. In *Treatise on Geochemistry*, vol. 3: *The Crust* (ed RL Rudnick), pp. 1–64. Oxford: Elsevier, Pergamon.
- Salvi S and Williams-Jones AE** (2005) Alkaline granite-syenite deposits. In *Rare-Element Geochemistry and Mineral Deposits: Short Course Notes* (eds RL Linnen and IM Samson), pp. 315–41. St John's: Geological Association of Canada, Special Publication no. 17.
- Sami M, Ntaflou T, Farahat ES, Mohamed HA, Hauzenberger C and Ahmed AF** (2018) Petrogenesis and geodynamic implications of Ediacaran highly fractionated A-type granitoids in the north Arabian-Nubian Shield (Egypt): constraints from whole-rock geochemistry and Sr–Nd isotopes. *Lithos* **304–307**, 329–46.
- Saunders AD, Tarney J, Marsh NG and Wood DA** (1980) Ophiolites as ocean crust or marginal basin crust: a geochemical approach. In *Ophiolites: Proceedings of the International Ophiolite Symposium, Cyprus, 1979* (ed. A Panayiotou), pp. 192–204. Nicosia: Ministry of Agriculture and Natural Resources Proceedings of the International Ophiolite Symposium, Cyprus.
- Schönenberger J, Köhler J and Markl G** (2008) REE systematics of fluorides, calcite and siderite in peralkaline plutonic rocks from the Gardar Province, South Greenland. *Chemical Geology* **247**, 16–35.
- Shaw DM** (1968) A review of K–Rb fractionation trends by covariance analysis. *Geochimica et Cosmochimica Acta* **32**, 573–601.
- Shaw DM** (1970) Trace-element fractionation during anatexis. *Geochimica et Cosmochimica Acta* **34**, 237–43.
- Sinclair WD** (2007) Porphyry deposits. mineral deposits of Canada: a synthesis of major deposit-types, district metallogeny, the evolution of geological provinces, and exploration methods. *Geological Association of Canada, Mineral Deposits Division, Special Publication no. 5*, 223–43.
- Singh J and Johannes W** (1996) Dehydration melting of tonalites. Part II. Composition of melts and solids. *Mineralogy and Petrology* **125**, 26–44.
- Stern RJ** (1994) Neoproterozoic (900–550 Ma) arc assembly and continental collision in the East African Orogen: implications for consolidation of Gondwanaland. *Annual Reviews of Earth and Planetary Science* **22**, 319–51.
- Stern RJ** (2018) Neoproterozoic formation and evolution of Eastern Desert continental crust: the importance of the infrastructure-superstructure transition. *Journal of African Earth Sciences* **18**, 15–27.
- Stern RJ and Ali KA** (2020) Crustal evolution of the Egyptian Precambrian rocks. In *The Geology of Egypt, Regional Geology Reviews* (eds Z Hamimi, A El-Barkooky, J Martínez Frias, F Harald & Y Abd El-Rahman), pp. 131–51. Cham: Springer Nature Switzerland..
- Stern RJ and Gottfried D** (1986) Petrogenesis of a Late Precambrian (575–600 Ma) bimodal suite in northeast Africa. *Contributions to Mineralogy and Petrology* **92**, 492–501.
- Stern RJ and Hedge CE** (1985) Geochronologic and isotopic constraints on late Precambrian crustal evolution in the Eastern Desert of Egypt. *American Journal of Science* **285**, 97–127.
- Strecheisen AL** (1974) Classification and nomenclature of Plutonic rocks: recommendation of the IUGS subcommission on the systematics of Igneous Rocks. *Geologische Rundschau* **63**, 773–86.
- Strecheisen AL** (1976) Classification of the common igneous rocks by means of their chemical composition: a provisional attempt. *Neues Jahrbuch für Mineralogie – Monatshefte* **1**, 1–15.
- Sylvester PJ** (1989) Post-collisional alkaline granites. *Journal of Geology* **97**, 261–80.
- Taylor SR and McLennan SM** (1985) *The Continental Crust: Its Composition and Evolution*. Oxford: Blackwell Scientific Publications, 312 pp.
- Taylor SR and McLennan SM** (1995) The geochemical evolution of the continental crust. *Reviews of Geophysics* **33**, 241–65.
- Thompson AB** (1996) Fertility of crustal rocks during anatexis. *Transactions of the Royal Society of Edinburgh: Journal of Earth Science* **87**, 1–10.
- Turner SP, Foden JD and Morrison RS** (1992) Derivation of A-type magmas by fractionation of basaltic magma: an example from the Padthaway Ridge, South Australia. *Lithos* **28**, 151–79.
- Wang L, Huang CC, Pang J, Zha X and Zhou Y** (2014) Paleofloods recorded by slackwater deposits in the upper reaches of the Hanjiang River valley, middle Yangtze River basin. *Journal of China Hydrology* **519**, 1249–56.
- Whalen JB, Currie KL and Chappell BW** (1987) A-type granites: geochemical characteristics, discrimination and petrogenesis. *Contributions to Mineralogy and Petrology* **95**, 407–19.
- White AJR and Chappell BW** (1983) Granitoid types and their distribution in the Lachlan Fold Belt, southeastern Australia. *Geological Society of America Memoirs* **159**, 21–34.
- Wilson M** (2007) *Igneous Petrogenesis*. London: Chapman and Hall, 411 pp.
- Wolf MB and Wyllie JP** (1994) Dehydration-melting of amphibolite at 10 kbar: the effects of temperature and time. *Contributions to Mineralogy and Petrology* **115**, 369–83.

- Wright TL and Doherty PC** (1970) A linear programming and least squares computer method for solving petrologic mixing problems. *Geological Society of America Bulletin* **81**, 1995–2008.
- Wu FY, Sun DY, Li H, Jahn BM and Wilde S** (2002) A-type granites in northeastern China: age and geochemical constraints on their petrogenesis. *Chemical Geology* **187**, 143–73.
- Yang JH, Wu FY, Chung SL, Wilde SA and Chu MF** (2006) A hybrid origin for the Qianshan A-type granite, northeast China: geochemical and Sr-Nd-Hf isotopic evidence. *Lithos* **89**, 89–106.
- Yeshanew FG** (2017) *Crustal evolution of the Arabian–Nubian Shield: insights from zircon geochronology and Nd–Hf–O isotopes*. PhD thesis, Stockholm University, Stockholm, Sweden., Published thesis.
- Zaraisky GP, Aksyuka AM, Devyatovaa VN, Udoratinab OV and Chevychelova VYU** (2009) The Zr/Hf ratio as a fractionation indicator of rare-metal granites. *Petrology* **17**, 25–45.
- Zen EA** (1986) Aluminium enrichment in silicate melts by fractional crystallization: some mineralogic and petrographic constraints. *Journal of Petrology* **27**, 1095–117.